



**HAL**  
open science

## Chemical tracers of a highly eccentric AGB-main-sequence star binary

T. Danilovich, J. Malfait, M. van de Sande, M. Montargès, P. Kervella, F. de Ceuster, A. Coenegrachts, T. J. Millar, A. M. S. Richards, L. Decin, et al.

### ► To cite this version:

T. Danilovich, J. Malfait, M. van de Sande, M. Montargès, P. Kervella, et al.. Chemical tracers of a highly eccentric AGB-main-sequence star binary. *Nature Astronomy*, 2024, 8, pp.308-327. <10.1038/s41550-023-02154-y>. <insu-04836889>

**HAL Id: insu-04836889**

**<https://insu.hal.science/insu-04836889v1>**

Submitted on 4 Oct 2025

HAL is a multi-disciplinary open access archive for the deposit and dissemination of scientific research documents, whether they are published or not. The documents may come from teaching and research institutions in France or abroad, or from public or private research centers.

L'archive ouverte pluridisciplinaire HAL, est destinée au dépôt et à la diffusion de documents scientifiques de niveau recherche, publiés ou non, émanant des établissements d'enseignement et de recherche français ou étrangers, des laboratoires publics ou privés.



Distributed under a Creative Commons CC BY 4.0 - Attribution - International License

# Chemical tracers of a highly eccentric AGB–main-sequence star binary

Received: 29 March 2023

Accepted: 30 October 2023

Published online: 3 January 2024

 Check for updates

T. Danilovich<sup>1,2,3</sup>✉, J. Malfait<sup>1</sup>, M. Van de Sande<sup>4</sup>, M. Montargès<sup>5</sup>, P. Kervella<sup>5</sup>, F. De Ceuster<sup>1</sup>, A. Coenegrachts<sup>1</sup>, T. J. Millar<sup>6</sup>, A. M. S. Richards<sup>7</sup>, L. Decin<sup>1,8</sup>, C. A. Gottlieb<sup>9</sup>, C. Pinte<sup>10,11</sup>, E. De Beck<sup>11</sup>, D. J. Price<sup>2</sup>, K. T. Wong<sup>12,13</sup>, J. Bolte<sup>14</sup>, K. M. Menten<sup>15</sup>, A. Baudry<sup>16</sup>, A. de Koter<sup>1,17</sup>, S. Etoka<sup>7</sup>, D. Gobrecht<sup>18</sup>, M. Gray<sup>7,19</sup>, F. Herpin<sup>16</sup>, M. Jesta<sup>15</sup>, E. Lagadec<sup>20</sup>, S. Maes<sup>1</sup>, I. McDonald<sup>7,21</sup>, L. Marinho<sup>16</sup>, H. S. P. Müller<sup>22</sup>, B. Pimpanuwat<sup>7,19</sup>, J. M. C. Plane<sup>8</sup>, R. Sahai<sup>23</sup>, S. H. J. Wallström<sup>1</sup>, J. Yates<sup>24</sup> & A. Zijlstra<sup>7</sup>

Binary interactions have been proposed to explain a variety of circumstellar structures seen around evolved stars, including asymptotic giant branch (AGB) stars and planetary nebulae. Studies resolving the circumstellar envelopes of AGB stars have revealed spirals, disks and bipolar outflows, with shaping attributed to interactions with a companion. Here we use a combined chemical and dynamical analysis to reveal a highly eccentric and long-period orbit for W Aquilae, a binary system containing an AGB star and a main-sequence companion. Our results are based on anisotropic SiN emission, the detections of irregular NS and SiC emission towards the S-type star, and density structures observed in the CO emission. These features are all interpreted as having formed during periastron interactions. Our astrochemistry-based method can yield stringent constraints on the orbital parameters of long-period binaries containing AGB stars, and will be applicable to other systems.

The asymptotic giant branch (AGB) is a late evolutionary stage of low- and intermediate-mass stars (–1 to 8 solar masses ( $M_{\odot}$ )). This stage is characterized by mass-losing stellar winds, rich in molecular gas and dust, which form an extended, expanding circumstellar envelope (CSE)

around the star<sup>1</sup>. AGB stars eventually transition through the planetary nebula phase and end as white-dwarf stars, having chemically enriched their host galaxies through their mass loss<sup>2</sup>. Binary companions can have a substantial impact on this process, potentially affecting

<sup>1</sup>Institute of Astronomy, KU Leuven, Leuven, Belgium. <sup>2</sup>School of Physics and Astronomy, Monash University, Clayton, Victoria, Australia. <sup>3</sup>ARC Centre of Excellence for All Sky Astrophysics in 3 Dimensions (ASTRO 3D), Clayton, Victoria, Australia. <sup>4</sup>School of Physics and Astronomy, University of Leeds, Leeds, UK. <sup>5</sup>LESIA, Observatoire de Paris, Université PSL, CNRS, Sorbonne Université, Université Paris Cité, Meudon, France. <sup>6</sup>Astrophysics Research Centre, School of Mathematics and Physics, Queen's University Belfast, Belfast, UK. <sup>7</sup>JBCA, Department Physics and Astronomy, University of Manchester, Manchester, UK. <sup>8</sup>School of Chemistry, University of Leeds, Leeds, UK. <sup>9</sup>Harvard-Smithsonian Center for Astrophysics, Cambridge, MA, USA. <sup>10</sup>Université Grenoble Alpes, CNRS, IPAG, Grenoble, France. <sup>11</sup>Department of Space, Earth and Environment, Chalmers University of Technology, Gothenburg, Sweden. <sup>12</sup>Theoretical Astrophysics, Department of Physics and Astronomy, Uppsala University, Uppsala, Sweden. <sup>13</sup>Institut de Radioastronomie Millimétrique, Saint-Martin-d'Hères, France. <sup>14</sup>Department of Mathematics, Kiel University, Kiel, Germany. <sup>15</sup>Max-Planck-Institut für Radioastronomie, Bonn, Germany. <sup>16</sup>Laboratoire d'Astrophysique de Bordeaux, Université de Bordeaux, Pessac, France. <sup>17</sup>Anton Pannekoek Institute for Astronomy, University of Amsterdam, Amsterdam, The Netherlands. <sup>18</sup>Department of Chemistry and Molecular Biology, University of Gothenburg, Gothenburg, Sweden. <sup>19</sup>National Astronomical Research Institute of Thailand, Chiangmai, Thailand. <sup>20</sup>Laboratoire Lagrange, Observatoire de la Côte d'Azur, Université Côte d'Azur, Nice, France. <sup>21</sup>School of Physical Sciences, The Open University, Milton Keynes, UK. <sup>22</sup>Physikalisches Institut, Universität zu Köln, Cologne, Germany. <sup>23</sup>Jet Propulsion Laboratory, California Institute of Technology, Pasadena, CA, USA. <sup>24</sup>Department of Computer Science, University College London, London, UK. ✉ e-mail: [taissa.danilovich@monash.edu](mailto:taissa.danilovich@monash.edu)

**Table 1 | Molecular lines in the ground vibrational state used in our analysis**

| Molecule           | Transition   | Frequency (GHz)      | Ref. for frequency | $u_{\text{cent}}$ (kms <sup>-1</sup> ) | Angular resolution (") | MRS (") | Recovered flux (%) |
|--------------------|--|----------------------|--------------------|--|------------------------|---------|--------------------|
| CO                 | $J=2 \rightarrow 1$                                  | 230.538              | 100                | -                                      | 0.132×0.123            | 5.3     | -                  |
|                    |  |                      |                    | -23.4                                  | 0.829×0.679            | 8.9     | 33                 |
| SiN                | $N, J, F=6, 13/2, 13/2 \rightarrow 5, 11/2, 11/2$    | 262.156 <sup>a</sup> | 26                 | -23.7                                  | 0.222×0.198            | 4.7     | 100                |
| SiC                | $^3\Pi_2, J=6 \rightarrow 5$                         | 236.288              | 57,101             | -23.8                                  | 0.199×0.184            | 2.6     | -                  |
| NS                 | $^2\Pi_{1/2}, f, F=11/2, 13/2 \rightarrow 9/2, 11/2$ | 253.968 <sup>b</sup> | 64                 | -                                      | 0.187×0.171            | 2.5     | -                  |
| HC <sub>3</sub> N  | $J=25 \rightarrow 24$                                | 227.419              | 102                | -22.5                                  | 0.204×0.181            | 5.4     | -                  |
|                    | $J=26 \rightarrow 25$                                | 236.513              | 102                | -21.8                                  | 0.208×0.191            | 2.6     | -                  |
|                    | $J=27 \rightarrow 26$                                | 245.606              | 102                | -21.4                                  | 0.213×0.172            | 5.0     | -                  |
|                    | $J=28 \rightarrow 27$                                | 254.700              | 102                | -20.8                                  | 0.190×0.172            | 2.5     | -                  |
| SiO                | $J=5 \rightarrow 4$                                  | 217.105              | 103                | -22.6                                  | 0.063×0.055            | 5.7     | 85                 |
| SiS                | $J=12 \rightarrow 11$                                | 217.818              | 104                | -21.4                                  | 0.063×0.055            | 5.7     | 91                 |
| CS                 | $J=5 \rightarrow 4$                                  | 244.936              | 105                | -22.5                                  | 0.078×0.066            | 5.0     | 79                 |
| HCN                | $J=3 \rightarrow 2$                                  | 265.886              | 106                | -23.0                                  | 0.061×0.053            | 2.4     | 72                 |
| H <sup>13</sup> CN | $J=3 \rightarrow 2$                                  | 259.012              | 107                | -22.2                                  | 0.073×0.064            | 4.8     | -                  |
| <sup>13</sup> CN   | $N, F_1, F_2, F=2, 0, 2, 3, \rightarrow 1, 0, 1, 2$  | 217.303 <sup>b</sup> | 108                | -                                      | 0.213×0.199            | 5.7     | 44                 |
|                    | $N, F_1, F_2, F=2, 1, 3, 4, \rightarrow 1, 1, 2, 3$  | 217.467 <sup>b</sup> | 108                | -                                      | 0.213×0.199            | 5.7     | 48                 |

<sup>a</sup>Frequency and corresponding quantum numbers of central hyperfine component are given. <sup>b</sup>Frequency and corresponding quantum numbers of the brightest hyperfine component are given. All frequencies are rest frequencies and all velocities are with respect to the local standard of rest. Column 4 lists the primary references that provide the measured frequencies and the spectroscopic designation of the transitions observed here. The Cologne Database for Molecular Spectroscopy<sup>108,110</sup> provides a comprehensive list of the best estimate of the transition frequencies, the excitation energies and the quantum mechanical line strengths. The quantum number  $F$  refers to the total angular momentum including nuclear spin; for <sup>13</sup>CN the quantum number  $F_1$  refers to the coupling of the electron spin angular momentum with the nuclear spin angular momentum of <sup>13</sup>C and  $F_2$  refers to the coupling of the rotational angular momentum ( $N$ ) with  $F_1$ ; for NS, the quantum number  $f$  refers to the upper  $\Lambda$  doubling component and is related to the parity of the level. Column 5 gives the central velocity of the line as obtained from fitting a soft parabola (see 'Data reduction' in 'ALMA results' in Methods). Column 7 gives the MRS for the ALMA observations.

mass-loss rates and chemistry<sup>3,4</sup>, and are thought to shape both the eventual planetary nebula<sup>5</sup> and the CSE during the AGB phase<sup>6</sup>. Binary stars with an AGB component are also the progenitors of various exotic objects, including barium stars, CH stars, extrinsic S-type stars and novae<sup>7</sup>. Hence, understanding binary systems containing AGB stars, especially through observations, is important for understanding their overall evolutionary progress, the initial–final mass relation and the evolution of their host galaxies.

Recent observations of some AGB stars have identified the signatures of binary companions imprinted in the structure of the CSE. In only a few cases, however, is the precise nature of the companion and its effects on the CSE known, thereby limiting the study of such systems. Systems with directly detected companions include Mira, which comprises an oxygen-rich AGB star and a white dwarf, in which the companion has contributed to the shaping of the CSE structure<sup>8,9</sup>, and L<sub>2</sub> Pup, an oxygen-rich AGB star surrounded by a disk with a planetary companion<sup>10</sup>. Bipolar structures around  $\pi^1$  Gru have been attributed to a recently detected close companion<sup>11</sup>, adding to the small number of AGB systems with directly detected companions. The spiral structures observed around the carbon stars AFGL 3068 and R Scl<sup>12–14</sup>, and the bipolar structures around the carbon star V Hya<sup>15</sup>, indicate the possible presence of binary companions that have not been directly detected. A more complete understanding of circumstellar structures will come from knowing both cause (for example, a stellar or planetary companion) and effect (the CSE structure) and should allow us to draw more direct links between AGB stars and planetary nebulae, which have been observed to show a multitude of complex asymmetric structures<sup>6,16</sup>.

W Aquilae (W Aql) is a binary system at a distance of 395 pc (see 'Distance' in Methods). It contains an S-type AGB star, which has a mixed carbon–oxygen chemistry ( $C/O \approx 1$ ) and may be transitioning from being oxygen rich to carbon rich, and an F9 main-sequence star<sup>17,18</sup> located to the southwest of the AGB star at a projected separation of  $\sim 0.5''$  (ref. 19). W Aql has been extensively studied through observations

taken with a variety of telescopes<sup>19–24</sup>. Spatially resolved observations of the polarized dust<sup>19</sup> and CO (ref. 22) around the AGB star have shown a large-scale asymmetry in the direction of the F9 companion, a sign that binary interactions may be shaping the CSE. However, the asymmetry exists at larger scales than the present separation of the two stars, from  $\sim 10''$  to  $\sim 100''$  (refs. 19, 20, 22). Some indications of spiral structure in the CSE were seen in observations taken by the Atacama Large Millimeter/submillimeter Array (ALMA) at a resolution of  $\sim 0.4''$  (ref. 22) but it was unclear whether these could be caused by the F9 star.

## Results

We have analysed high-resolution ALMA observations of the W Aql system with spatial resolutions of  $\sim 0.024''$ , that is, approximately twice the K-band stellar diameter<sup>25</sup>, and 40% larger than the millimetre stellar diameter (see 'AGB angular diameter' in Methods). We combined these with photometric observations, smoothed particle hydrodynamics (SPH) models and chemical kinetics models to put constraints on the orbit of the system. We have shown that all the observations are consistent with the hypothesis of a highly eccentric orbit, based primarily on the distributions of molecular species that formed during periastron passage and the structures seen in the CO observations, making such an interpretation highly probable.

### Species formed during periastron passage

From a detailed examination of the ALMA data (see 'ALMA results' in Methods), we identified several molecules showing spatially asymmetric emission (details of molecular transitions are given in Table 1). Most notable was SiN, which has been detected towards only one other AGB CSE<sup>26</sup>. In Fig. 1a, we plot a zeroth-moment (integrated intensity) map of SiN, which shows emission in a roughly triangular wedge mainly to the northeast of the AGB star. To further understand the spatial origin of the emission, we constructed a position–velocity diagram (Fig. 1b), which reveals an arc of SiN emission that lies side-on ( $90^\circ$ ),

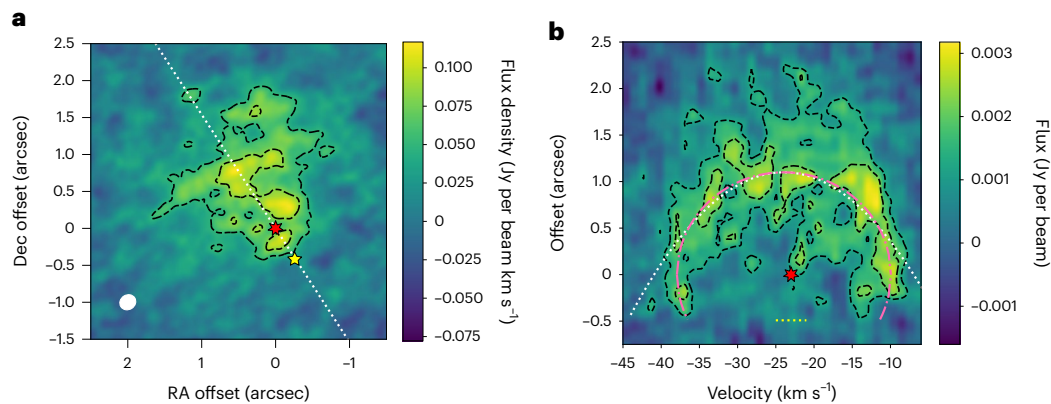


**Fig. 1 | Observed SiN emission towards W Aql. a**, Zeroth-moment map of SiN ( $N, J = 6, 13/2 \rightarrow 5, 11/2$ ) towards W Aql with contours at levels of  $3\sigma$  and  $5\sigma$ . The position of the AGB star is indicated by the red star at (0, 0) and the current location of the F9 star is indicated by the yellow star to the southwest. North is up and east is to the left. The dotted white line indicates the axis used for the position–velocity diagram in **b** and the white ellipse in the bottom left corner indicates the size of the synthesized beam. **b**, Position–velocity diagram of SiN

towards W Aql, taken at a position angle of north  $33^\circ$  east, as indicated by the dotted white line in **a**. Dashed black contours are at levels of  $3\sigma$  and  $5\sigma$ , a dotted white parabola is fit to the data (see ‘SiN and SiC’ in ‘ALMA results’ in Methods) and a dash-dotted pink ellipse is plotted to emphasize the shape of the emission in the position–velocity diagram. The position and LSR velocity ( $v_{\text{LSR}} = -23 \text{ km s}^{-1}$ ) of the AGB star is indicated by the red star and the horizontal yellow dotted line indicates the present offset of the F9 star. Dec, declination; RA, right ascension.

that is, perpendicular to the plane of the sky (see ‘SiN and SiC’ under ‘ALMA results’ in Methods).

The absence of (approximate) spherical symmetry in the emission suggests a spatial and/or temporal dependence for the formation of SiN around W Aql. Chemical kinetics models indicate that the production of SiN is higher in the presence of ultraviolet (UV) photons—such as can be provided by a main-sequence companion<sup>4</sup> like the F9 component of W Aql, but only in sufficiently dense regions of the CSE (see ‘Chemical modelling’ in Methods for further details of the chemistry initiated by the companion’s UV field). We posit that: (1) the binary orbit is highly eccentric and inclined  $i \approx 90^\circ$ ; (2) the formation of the arc of SiN was triggered close to periastron (Fig. 2 and Extended Data Fig. 1), when the F9 star passed close to the AGB star and irradiated part of the dense inner AGB wind; and (3) this temporarily drove chemical reactions through increased (but not complete) photodissociation and photoionization, including those reactions that led to the formation of SiN (see ‘SiN and SiC’ under ‘Chemical modelling’ in Methods). We used radiative transfer modelling to estimate the abundance of SiN in the arc and found a peak abundance of  $1.5 \times 10^{-7}$  relative to  $\text{H}_2$  (see ‘Radiative transfer modelling’ in Methods), which is in general agreement with the expectations from chemical models containing an F9-like companion. Further evidence in support of this formation mechanism is provided by the presence of SiC and NS emission towards W Aql. Their emission is also distributed asymmetrically (with a weaker signal-to-noise ratio (SNR) than SiN; see ‘SiN and SiC’ and ‘NS’ under ‘ALMA results’ in Methods, and Extended Data Figs. 2 and 3). The presence of SiC and NS is consistent with chemical model predictions<sup>4</sup> for the effect of the periastron passage of the F9 star on the chemistry of the CSE (see ‘SiN and SiC’ and ‘NS’ under ‘Chemical modelling’ in Methods).

### Photodissociation of common species

Farther from the AGB star, such as where the F9 star is currently located, the wind is less dense ( $\sim 3 \times 10^5 \text{ cm}^{-3}$  compared with  $\sim 10^9 \text{ cm}^{-3}$  at 10 au from the AGB star) and the chemistry tends to be initiated by photodissociation by the interstellar radiation field. The density in this region is too low for species such as SiN to form; however, we see evidence of the F9 star driving additional photodissociation in the zeroth-moment maps of SiO, SiS, CS and HCN (Fig. 3), all of which show extended emission to the northeast and truncated emission to the southwest, in the direction of the present position of the F9 star. The central channels of

SiS and CS, in particular, show significantly lower molecular emission around the F9 star (Extended Data Fig. 4). Spectra centred on the current position of the F9 star show very few detected molecular lines and the line profiles of CS, SiO and HCN show less emission around the local standard of rest (LSR) velocity compared with spectra centred on the AGB star or at the same distance from the AGB star but on the opposite side of the CSE (see ‘Molecular emission around F9 star’ under ‘ALMA results’ in Methods and Extended Data Fig. 5).

Additional evidence of the F9 star driving photodissociation is found by comparing the distribution of  $\text{H}^{13}\text{CN}$  with the distribution of  $^{13}\text{CN}$  (note,  $^{12}\text{CN}$  was not covered by our observations), because CN is a photodissociation product of  $\text{HCN}^{27}$ . As shown in Fig. 4,  $^{13}\text{CN}$  is found to be present mainly in the region in which the  $\text{H}^{13}\text{CN}$  emission is truncated. This is consistent with the F9 star driving the photodissociation of  $\text{H}^{13}\text{CN}$  and hence creating  $^{13}\text{CN}$ . We also plot the zeroth-moment map of the  $J = 27-26$  transition of  $\text{HCCCN}$  (where  $J$  is the quantum number referring to the total angular momentum excluding nuclear spin and  $\text{HCCCN}$  is the next member in the cyanopolyne family, hereafter  $\text{HC}_3\text{N}$ ; Fig. 4), which shows emission on the same side of the AGB star as  $^{13}\text{CN}$ , albeit over a much smaller region. The other observed transitions of  $\text{HC}_3\text{N}$  show a similar distribution (Extended Data Fig. 6). Because  $\text{HC}_3\text{N}$  forms from CN (see ‘HCN, CN and  $\text{HC}_3\text{N}$ ’ under ‘Chemical modelling’ in Methods), its asymmetric distribution indicates an asymmetric CN distribution and hence provides further evidence of anisotropic photo-processes in the CSE.

### Structures in CO emission

CO is an abundant stable molecule, commonly used as a density tracer in CSEs. We plot high-resolution ( $0.132'' \times 0.123''$ ) channel maps of CO emission in Extended Data Fig. 7 and first focus on the central three channels closest to the AGB stellar velocity  $v_{\text{LSR}} = -23 \text{ km s}^{-1}$  (Fig. 5a). With the aid of angle–radius plots (Extended Data Fig. 8), we identified two key circular structures in the CO emission, with radii of  $1.35''$  and  $10.75''$ , with centres offset from the present position of the AGB star by  $0.1''$  and  $1.5''$  to the north. These are shown in black and white in Fig. 5a. Other circular structures are highlighted in red and pink and, because these are offset to the southwest, we presume that they were formed through different processes to the black and white circles and focus on the latter first.

To better understand the origin of the circular structures, we performed hydrodynamic simulations for highly eccentric systems

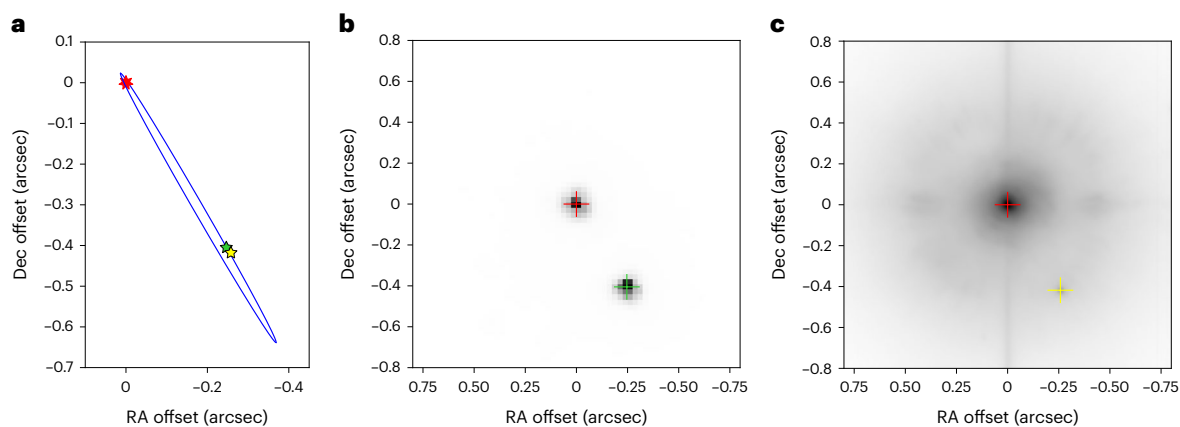


**Fig. 2 | Plots of the orbit of the W Aql system as seen in the plane of the sky.** In all panels, north is up and east is left. The orbital parameters shown are for eccentricity  $e = 0.93$  and periastron separation  $r_p = 1.5 \times 10^{14}$  cm. Although we find the inclination to be  $i = 90 \pm 7^\circ$ , we plot the orbit with  $i = 85^\circ$  so that it is possible to see the ellipse. **a**, Plot of the orbit of the W Aql system in the frame of the AGB star. The location of the AGB star is shown as a red star at (0, 0), the position of the F9 star from the SPHERE observation is shown as a yellow star and from the

HST observation as a green star. **b**, B-band image of W Aql observed with HST in 2004<sup>19</sup>, plotted with a linear intensity scale. The measured centres of the AGB and F9 stars are indicated with the red and green crosses, respectively. **c**, VLT/SPHERE-ZIMPOL image of W Aql in the VBB filter, observed in 2019<sup>48</sup>, plotted with a logarithmic intensity scale. The measured centres of the AGB and F9 stars are indicated with the red and yellow crosses, respectively.

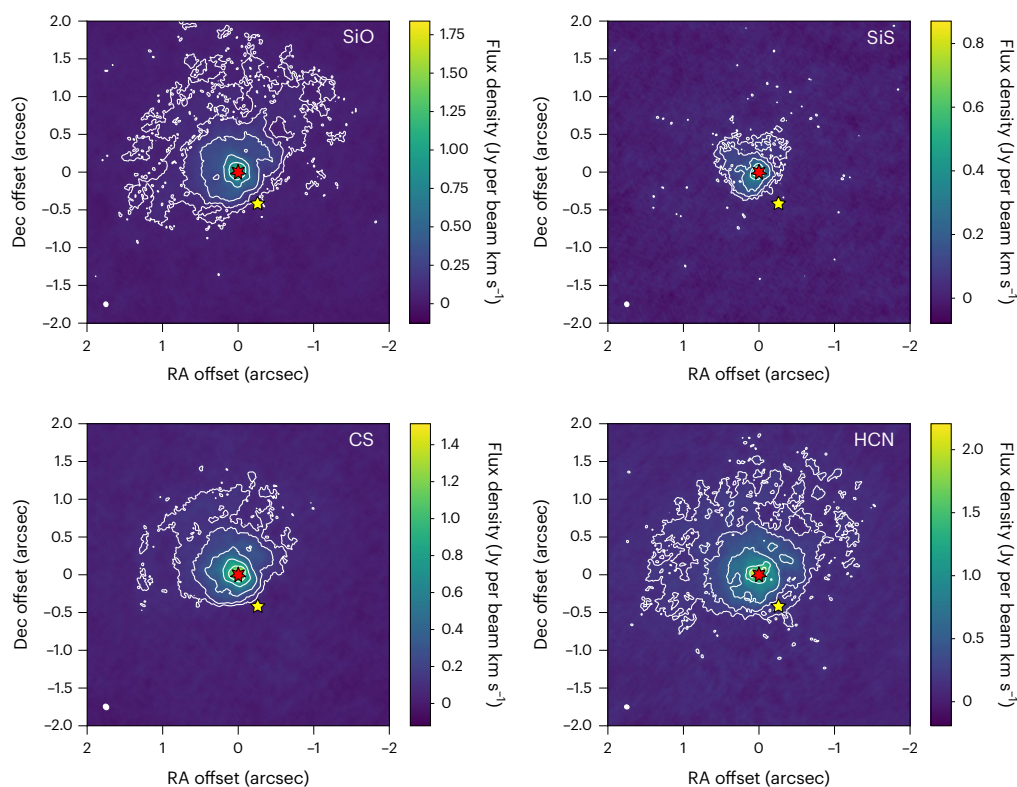


**Fig. 3 | Observed SiO, SiS, CS and HCN emission towards W Aql.** Zero-moment maps are shown for the transitions given in Table 1. White contours are at levels of  $3\sigma$ ,  $5\sigma$ ,  $10\sigma$ ,  $20\sigma$  and  $30\sigma$ . The position of the AGB star is indicated by

the red star at (0, 0) and the location of the F9 companion is indicated by the yellow star to the southwest. North is up and east is left. The white ellipses in the bottom left corners indicate the sizes of the synthesized beams.

based on the W Aql system (details in ‘Hydrodynamic simulations’ in Methods). From these, we found that highly elliptical orbits ( $e \geq 0.8$ ) result in almost spherical structures in the wind, which appear circular and slightly offset away from the present position of the companion when viewed edge-on ( $i = 90^\circ$ ) relative to the plane of the orbit (Fig. 5c). These structures are generated during periastron passages and are very similar to the black and white circles seen in the ALMA CO data, even

more so when the hydrodynamical model is processed with a radiative transfer code (Fig. 5d). The fact that the outer edge of the SiN emission overlaps with the inner circular structure (Fig. 5b) also suggests that they were formed contemporaneously, that is, during the most recent periastron passage. We also determined that the different emission distributions seen in the blue (elongated) and red (circular) channels of our ALMA observations are reproduced in the hydrodynamic model

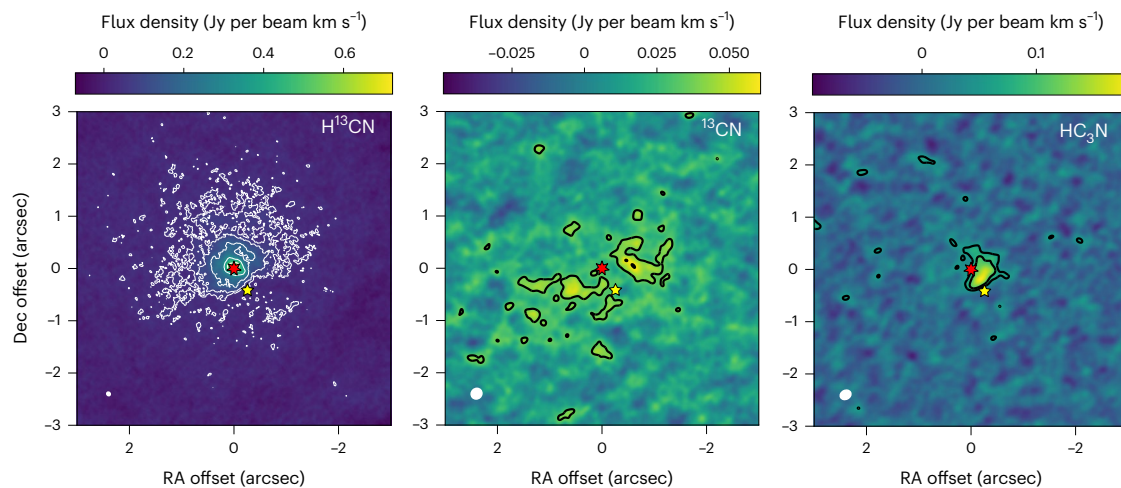


**Fig. 4 | Observed emission of CN-bearing molecules towards W Aql.** Zero-moment maps of  $\text{H}^{13}\text{CN}$  (left),  $^{13}\text{CN}$  (centre) and  $\text{HC}_3\text{N}$  ( $J = 27 \rightarrow 26$ , right) towards W Aql. Full transition details are given in Table 1. Contours are at levels of  $3\sigma$  and  $5\sigma$ , and additionally  $10\sigma$ ,  $20\sigma$  and  $30\sigma$  for  $\text{H}^{13}\text{CN}$ . The position of the AGB

star is indicated by the red star at (0, 0) and the location of the F9 companion is indicated by the yellow star to the southwest. North is up and east is left. The white ellipses in the bottom left corners indicate the sizes of the synthesized beams.

(Extended Data Fig. 9). On the basis of all of these results, we can constrain the orbital parameters of the W Aql system.

### Orbital parameters

From the circular structures seen in Fig. 5, we estimate the orbital period to be  $1,082^{+89}_{-108}$  years. On the basis of the expansion time of the inner circle and the arc of SiN, we estimate the time since the most recent periastron to be  $172 \pm 22$  years (see ‘Orbital parameters from ALMA observations’ in Methods). The SiN position–velocity diagram indicates an orbital inclination of  $i = 90 \pm 7^\circ$  (see ‘SiN and SiC’ under ‘ALMA results’ in Methods). Combining these results with resolved images of W Aql (see ‘Spatially resolved imaging’ in Methods), we found a series of numerical solutions that reproduce the observations within their uncertainties (see ‘Orbital solutions’ in Methods). All our solutions (Extended Data Table 1) have high eccentricities ( $e > 0.9$ ) and small periastron distances ( $r_p \leq 2 \times 10^{14}$  cm = 13 au), with long periods  $\sim 1,100$  years. A solution with  $e = 0.93$ ,  $r_p = 1.5 \times 10^{14}$  cm (10 au) and period 1,051 years is plotted in Fig. 2, where it is superposed on resolved images to show the agreement with the positions of the stars.

### Discussion

We have identified in observations, with the aid of astrochemistry, molecular species that formed during a periastron passage of an AGB + main-sequence (F9) binary system. Through our analysis of these species, in combination with structures in the CO and resolved images of the two stars, we were able to constrain the binary orbit to a limited number of solutions, all having high eccentricities and almost edge-on inclinations. Our analysis demonstrates a method for studying binary systems containing AGB stars by observing spatially resolved emission of key molecular species.

SiN was crucial to our analysis because it is distributed asymmetrically in the W Aql CSE—alerting us to a non-standard formation pathway—and was detected with a sufficiently high SNR to be readily analysed. The other two molecules that we identified as being created during periastron, SiC and NS, strengthened our argument but their lower SNR in the present observations would not have allowed us to draw firm conclusions in the absence of SiN. However, we note that all three molecules have the potential to serve as diagnostic tools for identifying binary interactions in other systems, especially with targeted observations at high SNR. On the basis of the predictions of chemical models that consider the presence of a Sun-like companion<sup>4</sup>,

SiN and SiC are expected to be good tracers of stellar companions to S-type and oxygen-rich AGB stars, but probably not carbon stars (unless notably asymmetric emission is detected), because carbon-rich CSEs are expected to have higher abundances of both molecules without the presence of a companion. NS is predicted to have higher abundances around carbon stars in the presence of a white-dwarf companion, but not if the companion is a main-sequence star. For S-type and oxygen-rich AGB stars, NS is expected to be a good tracer of either a white-dwarf or a Sun-like companion. While there may be other molecules that are enhanced or destroyed in the presence of a companion, a comprehensive list is difficult to compile<sup>4</sup>. After checking all detected molecular lines for asymmetries, we do not find any additional candidates for tracers of binary-induced chemistry towards W Aql.

The timing between our observations and the present orbital configuration of W Aql contributed to our being able to use SiN to characterize the orbit. If the W Aql system was instead observed  $\sim 200$  years before the next periastron, rather than  $\sim 200$  years after the most recent periastron, it is unlikely that SiN would have been detected. In that case, in the  $\sim 900$  years since the previous periastron, the SiN arc would have expanded with the CSE to around 4 times farther from the AGB star than what we currently observe. At that radial distance, most of the SiN would have been destroyed through photodissociation by the interstellar radiation field<sup>4</sup>. This is also why we do not detect SiN that was created contemporaneously with the white circle in CO (Fig. 5a) during the second most recent periastron passage,  $\sim 1,300$  years ago. That said, SiN has already persisted for  $\sim 200$  years since the periastron interaction, and may continue to be detectable for another 50 to 100 years, based on the expansion velocity and excitation conditions. This means that the imprint of the periastron interaction will be potentially detectable for around a quarter of the total orbital period, a much larger portion than if we had to rely on, for example, observing changing stellar positions or radial velocities around periastron (Extended Data Table 1). The high eccentricity and small periastron separation of the system also contributed to favourable conditions for the formation of SiN around W Aql. As noted above and in ‘Chemical modelling’ in Methods, the companion-initiated photochemistry is most impactful in the dense inner CSE, meaning that the tracers of this photochemistry—SiN, SiC and NS—may not be formed in sufficiently high quantities to be detected for binary systems with wider orbits, where the companion passes through regions of the CSE with lower number densities. Despite these potential limitations, molecular tracers in the CSE generally

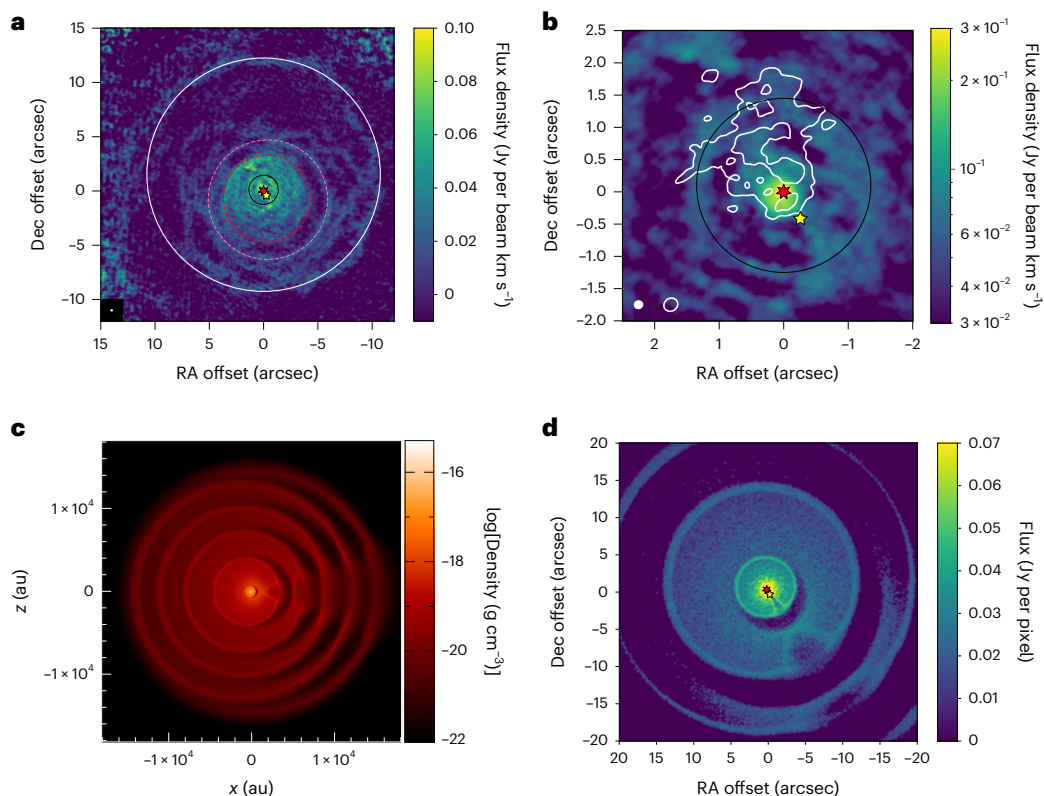


**Fig. 5 | Observations and simulations of CO emission towards W Aql.** **a**, A plot of the three central CO channels observed with ALMA summed together (see channels highlighted in Extended Data Fig. 7). We include circles (white, black, red, pink) to guide the eye to structures in the emission. The location of the AGB star is shown as a red star and the present location of the companion is shown as a yellow star. North is up and east is left. The synthetic beam size is shown as a white ellipse including a black square in the bottom left corner. **b**, The same as the central part of **a**, including the black circle, but plotted on a logarithmic colour scale to emphasize structure. The white contours are the SiN zeroth-moment map as shown in Fig. 1a. The filled ellipse in the bottom left corner shows the synthetic beam for the CO data and the unfilled ellipse is the synthetic beam of the SiN data.

**c**, Density distribution in a two-dimensional slice through a plane perpendicular to the orbital plane ( $y = 0$ ), similar to the edge-on orientation of the W Aql system, from a three-dimensional SPH model with masses  $M_{\text{AGB}} = 1.6 M_{\odot}$  and  $M_2 = 1.06 M_{\odot}$ , eccentricity  $e = 0.92$ , and semimajor axis  $a = 125$  au. The barycentre of the system is located at 0, 0 and at the scale plotted ( $1 \times 10^4$  au  $\approx 25''$ ) the AGB and F9 stars cannot be distinguished. See ‘Hydrodynamic simulations’ in Methods for more details. **d**, The central channel of **c** after processing with a radiative transfer model to convert the model density to CO ( $2 \rightarrow 1$ ) intensity, taking photodissociation into account (see ‘Hydrodynamic simulations’ in Methods for details). Star positions are taken from the model in **c**.

persist for a relatively long time (hundreds of years, depending on the molecule) and allow us to probe the system on longer timescales than direct imaging or radial velocity measurements, which can be taken on only human timescales. Hence, molecular tracers are invaluable for constraining binary systems with long orbital periods.

The W Aql system may be unusual for having such a highly eccentric orbit, but it is not unique nor is it impossible for it to have formed with such a high eccentricity. In fact, studies of eccentricity distributions that include wider binaries find a tendency for the mean eccentricity to be higher for subsamples with larger periods<sup>28,29</sup>. Indeed, for long-period binaries, orbital circularization during their formation is not expected<sup>30</sup>. Furthermore, a large statistical analysis of binary systems found that solar-type stars in binaries are more likely to have long periods than short periods, that is, the companion frequency distribution for solar-type primaries peaked at periods of  $\log[P(\text{days})] = 5.5$  (ref. 30), very close to the period we found for W Aql ( $\log[P_{\text{WAql}}(\text{days})] = 5.6$ ). Both the aforementioned studies focused primarily on main-sequence stars, but our result for W Aql shows that wide binaries with high eccentricities can survive to the AGB phase. Our hydrodynamic model, which takes into account the gravitational effect of the secondary star on the wind and vice versa, shows a very slightly increasing orbital period (owing to the mass lost by the AGB star) but negligible changes in eccentricity, and does not show precession over

~5,000 years. While 5,000 years may seem too short a time to make a definitive judgement, we point out that the expansion of the CSE during this time represents a larger spatial extent than the cool dust emission imaged by the Herschel Photoconductor Array Camera and Spectrometer (at 70  $\mu\text{m}$  and 160  $\mu\text{m}$  (ref. 20)). Despite the high eccentricity that we find for W Aql, none of our orbital solutions (Extended Data Table 1) have periastron separations smaller than the Roche limit, so no direct interaction between the two stars is expected and no evidence of such an interaction is seen in the ALMA observations. This suggests a relatively stable, if slowly evolving, system from which we could expect the eventual formation of a planetary nebula characterized by elongation to the southwest and perhaps a variety of additional arcs, analogous to what is currently seen in the AGB CSE, including at larger scales<sup>19,20,22</sup>.

Other binary systems containing AGB stars have also been found to have long periods (based mainly on spiral-like structures in CO observations) including AFGL 3068 (~800 years<sup>13</sup>), R Scl (445 years<sup>14,31</sup>) and II Lup (128 years<sup>32</sup>). In comparison, AGB stars that have close companions, such as  $\pi^1$  Gru (current projected separation 6 au (refs. 11,33), period unknown) and V Hya (period of 8.5 years<sup>15,34</sup>), both of which are triple systems that also have wide companions, have less spherical and more disrupted CSEs with, for example, bipolar outflows. Unlike the former group with more spherical CSEs, these triple systems are

more likely to go on to form bipolar planetary nebulae. The very high eccentricity of W Aql precludes the presence of a stable third companion and, despite the small periastron separation, we can consider it to be a relatively undisrupted system, suggesting the eventual formation of a relatively regular planetary nebula, that is, perhaps more closely resembling the Ring Nebula than the Butterfly Nebula.

The study we have presented here adds to the small number of AGB stars with known companions and orbital parameters. While previous studies have struggled to explain the range of eccentricities observed for, for example, post-AGB stars, most of these have focused on shorter orbital periods, ranging up to 1,000 days, rather than 1,000 years, owing to observational limitations<sup>35</sup>. The W Aql system provides further evidence that highly eccentric systems with long orbital periods exist during the AGB phase and that such eccentricity could be inherited by binary systems in later evolutionary phases, such as post-AGB stars and barium stars<sup>36</sup>. The method used here—which entails the combination of chemical tracers and hydrodynamical models—can be used to detect the characteristic effects of main-sequence binary companions in other AGB CSEs. Rather than solely searching for structures in the CSE, future studies can also check for anisotropies in molecular emission and the production of particular molecular species to confirm or rule out the presence of a stellar companion.

## Methods

### Distance

Many of the measurements and calculations in the present work rely on the value of the distance to the W Aql system and, more specifically, to the AGB component. Previous modelling of W Aql has assumed a distance of 395 pc, calculated from a period–magnitude relation<sup>21</sup>. Before this, a variety of distances were assumed for W Aql, ranging from 230 pc to 680 pc (refs. 37–40). Recently, distances have been calculated based on high-precision parallax observations from the Gaia mission<sup>41</sup>. Values of  $374 \pm 22$  pc (ref. 24) and  $380_{-49}^{+68}$  pc (ref. 42) were found using different methods based on the Gaia Early Data Release 3<sup>43</sup>. In this work, we continue to use a distance of 395 pc because this value falls within the uncertainties of both Gaia-derived values, and because it has been previously used in many radiative transfer models for the AGB star<sup>21–24</sup> and various stellar and circumstellar parameters such as luminosity and mass-loss rate have been derived relative to this value (Supplementary Table 1). We note that if the true distance is not exactly the adopted one, then the derivations of various parameters would be altered in the following way: mass-loss rate and relative molecular abundances would tend to increase for a larger distance, although molecular abundances may not change significantly after the mass-loss rate was updated, owing to a degeneracy between the impact of distance and density (the latter being directly related to mass-loss rate) on the line intensity. Our derived projected separations would increase linearly with distance, which would in turn result in a larger calculated orbital period.

### Stellar masses

The companion to the AGB star was identified as a main-sequence star classified as F8 to G0<sup>18</sup>, implying that the stellar mass is in the range  $1.09$ – $1.04 M_{\odot}$  (ref. 44). For the purposes of this study, we have assumed the companion is an F9 star with a mass of  $1.06 M_{\odot}$ .

The situation for the AGB component is more complicated. Previous studies comparing oxygen isotopic ratios with stellar evolution models have calculated an initial stellar mass for the AGB star of  $1.6 \pm 0.2 M_{\odot}$  (refs. 45,46). Although the current mass-loss rate of the AGB star is relatively high at  $\dot{M} = 3 \times 10^{-6} M_{\odot} \text{ yr}^{-1}$  (ref. 22), stellar evolution models indicate that a significant decrease in stellar mass (that is,  $>0.1 M_{\odot}$ ) is not expected to occur until the final stages of the thermally pulsing AGB phase (that is, during and after the last one or two thermal pulses<sup>47</sup>). Ergo, we assume  $1.6 M_{\odot}$  for the present AGB mass and hence assume a total system mass of  $2.66 M_{\odot}$ .

### Spatially resolved imaging

W Aql was observed with the Advanced Camera for Surveys (ACS) on the Hubble Space Telescope (HST) at 400 nm on 12 October 2004 (Fig. 2b)<sup>19</sup>. It was observed again with the Very Large Telescope instrument Spectro-Polarimetric High-contrast Exoplanet REsearch Zurich Imaging Polarimeter (VLT/SPHERE-ZIMPOL) at 735.4 nm on 9 July 2019 (Fig. 2c)<sup>48</sup>. Both HST and SPHERE images were taken during a similar phase of the AGB pulsation, approximately halfway between maximum and minimum light. Another HST observation was taken with the Wide Field/Planetary Camera (WFPC) at 550 nm in 1993<sup>20</sup>, but this was taken before the first servicing mission, and the degraded angular resolution makes it unusable for our study.

We measured the positions of the AGB and F9 stars using the Python package `lmfit` (<https://lmfit.github.io/lmfit-py/index.html>). We find the separation between the two stars is  $475 \pm 1.0$  mas in the HST epoch, and  $491 \pm 1.8$  mas in the SPHERE epoch. For HST, the astrometry is well characterized and the uncertainties were estimated based on the noise of the images. For SPHERE, the astrometric uncertainty includes the orientation with respect to north, the distortion, the plate-scale stability and the statistical position uncertainty<sup>49</sup>. The change in projected distance between the two stars is then calculated to be  $16 \pm 0.25 \pm 1.79$  mas (to distinguish between the systematic and statistical uncertainties) in 14.75 years, with the projected motion of the F9 star approximately following a straight line away from the AGB star. This motion does not contradict a highly inclined, nearly edge-on orbit, with inclination,  $i \approx 90^{\circ}$ . The 2019 SPHERE position corresponds to a projected separation of 194 au, at our adopted distance of 395 pc.

These results indicate that the orbital period must be long, particularly compared with the timescale of our observations. For example, a circular orbit with a radius of 194 au gives a period of 1,660 years for our assumed system mass of  $2.66 M_{\odot}$ . An extremely elliptical orbit with an apastron of 194 au and a periastron of 3 au (a value chosen so that the F9 star does not pass through the AGB star, as we see no evidence of such an extreme interaction) results in a period of 600 years. Note that neither of these orbits properly consider the motion seen between the HST and SPHERE epochs and are merely illustrative. The ephemeris of such a long orbit cannot be constrained through direct photometric imaging in a reasonable timeframe, because the observations would need to be taken decades and centuries apart. Hence, we require other markers in the circumstellar environment of the AGB star to constrain the orbital parameters of the W Aql system.

### ALMA results

High-spatial-resolution observations of W Aql were obtained with ALMA as part of the ATOMIUM Large Programme (ALMA Tracing the Origins of Molecules In dUst-forming oxygen-rich M-type stars; programme ID 2018.1.00659.L; principal investigator L. Decin)<sup>50</sup>. More than 110 molecular lines were detected towards W Aql, including CO, SiN, SiC, NS and HC<sub>3</sub>N, which are analysed here. Previously, SiN was detected and HC<sub>3</sub>N was tentatively detected towards W Aql with the Atacama Pathfinder EXperiment (APEX) telescope<sup>46</sup>, which does not provide spatial information. Here we present observations of spatially resolved emission of all studied molecules. The SiN, SiC and HC<sub>3</sub>N emission show two types of asymmetric morphology, both different to the more extensive circumstellar structures revealed by the CO observations at high spatial resolution.

**Data reduction.** W Aql was observed with three array configurations of ALMA. This enabled us to observe small structures at high angular resolutions (down to  $0.024'' \times 0.021''$ ) while still retrieving larger structures (up to a maximum recoverable scale (MRS) of  $8.9''$ ) that would otherwise be resolved out<sup>50</sup>. While these are the extremes of resolution and MRS available in the ATOMIUM dataset, the precise properties of the data we analyse can be found in Table 1 for each transition.

We combined the three datasets to maximize the sensitivity of images, using the Common Astronomy Software Applications for Radio Astronomy<sup>51</sup>. We used the combined data to make spectral image cubes for each transition in Table 1, weighting the contributions of the baselines to optimize the resolution and surface brightness sensitivity. The velocity resolution is 1.1–1.3 km s<sup>-1</sup> depending on frequency, and in some cases we averaged 2 or more channels to increase sensitivity. The typical root-mean-square (rms) noise is  $\lesssim 2$  mJy. All velocities are adjusted to the LSR frame. The relative astrometric accuracy of the extended configuration alone is  $-0.002''$  and  $-0.005''$  for the combined data at slightly lower resolution. The flux scale for the combined images is accurate to  $\sim 10\%$ . The chances of interferometric noise causing artefacts  $\geq 5\sigma$  in these images is negligible. The relative position accuracy of measurements is at least equal to the synthesized beam divided by the SNR<sup>52</sup>, so for SNR = 5 this is  $\sim 40$  mas for SiN, SiC, NS, HC<sub>3</sub>N and <sup>13</sup>CN, around 25 mas for CO, and 12 mas for SiO, SiS, CS and HCN.

Moment-zero (integrated intensity) maps were made by summing all the channels with emission above  $-3\sigma_{\text{rms}}$ . Position–velocity diagrams were made by selecting a tilted rectangular slice (‘slit’) covering the moment-zero emission (spanning a width of  $3''$ ) at the angle shown in Fig. 1 (although other angles were tested, see ‘SiN and SiC’ below), and measuring the flux density in this region for each channel in increments along the slice. The peak of the continuum emission was assumed to be the position of the AGB star. In the channel maps and moment-zero maps, the position of the AGB star is at (0, 0). A small secondary peak, associated with the position of the F9 star, was detected in the continuum emission and will be analysed in a future paper.

To check whether our observations suffered from resolved-out flux, we compared spectra extracted from the ALMA data with previous observations of the same lines taken with the APEX single antenna<sup>46</sup> as shown in Supplementary Fig. 1. For CO, we found that 66% of the flux was resolved out, whereas all the flux was recovered by ALMA for SiN. We were unable to make the same comparison for SiC, which has not been detected with APEX, or HC<sub>3</sub>N, which was at best only tentatively detected with APEX<sup>46</sup>. Although only a third of the CO flux was recovered by ALMA, it is only smooth large-scale flux that is resolved out. This large-scale flux is mostly associated with smoother bulk outflows, whereas our analysis in the present work focuses on smaller structures in the wind—that is, the missing CO flux does not impede the present study.

Out of the other molecular lines discussed here and which have previously been observed, we found that about 28% of the flux in H<sup>12</sup>CN  $J = 3 \rightarrow 2$  was resolved out (Supplementary Fig. 2). Some degree of lost flux was expected because this line was not observed with the most compact configuration of ALMA. The corresponding transition in H<sup>13</sup>CN was not observed with APEX<sup>46</sup> but as it was observed with the compact configuration of ALMA and shows more extended emission than H<sup>12</sup>CN, we can assume very little, if any, flux was resolved out for H<sup>13</sup>CN. For SiO, SiS and CS, most of the flux was recovered, with only about 10–20% lost, as can be seen in Supplementary Fig. 2, where we have compared the spectra of these three molecules and H<sup>12</sup>CN observed with APEX and ALMA.

The <sup>13</sup>CN emission in  $N = 2 \rightarrow 1$  at 217 GHz (where  $N$  is the quantum number referring to the rotational angular momentum) has a low SNR. Therefore, to better determine the spatial distribution of <sup>13</sup>CN, we combined the two most intense components of the many possible fine- and hyperfine-structure transitions of the  $N = 2 \rightarrow 1$  transition that span a 450 MHz wide range centred on 217.257 GHz. We extracted the channels in the calibrated visibility data in the frequency ranges corresponding to  $v_{\text{LSR}} = -23 \pm 50$  km s<sup>-1</sup> around each of the rest frequencies and combined the channel selections aligned in velocity. The combined dataset was assigned a fictitious rest frequency of 217.3055 GHz so that its central velocity corresponded to  $-23$  km s<sup>-1</sup>, and we then made an image cube from the stacked visibility data and analysed this following the same procedure as for the other data cubes. Finally, we checked

the two multiplets of <sup>13</sup>CN listed in Table 1 individually for resolved-out flux and found that a little less than half of the flux was recovered for these lines.

For all the spectral lines studied here, except for <sup>13</sup>CN and NS, we fit soft parabola profiles<sup>53</sup>

$$F(v) = F_0 \left( 1 - \left[ \frac{v - v_{\text{cent}}}{v_{\infty}} \right]^2 \right)^{\gamma/2} \quad (1)$$

where  $v_{\text{cent}}$  is the central velocity of the line profile and  $F_0$  is the flux at the centre of the line. The parameters  $F_0$ ,  $v_{\text{cent}}$ ,  $v_{\infty}$  and  $\gamma$  are left as free parameters in the fit. Primarily, this is done to obtain the central line velocities, which are included in Table 1. The soft parabola profile was chosen over a Gaussian profile because the majority of the lines studied here show double-peaked emission and hence significantly deviate from Gaussian line profile shapes. <sup>13</sup>CN was excluded from this analysis because its hyperfine structure dominates its line profile, and NS was excluded because the spectrum is too noisy to obtain a reasonable fit. The central velocities of the lines were generally in agreement with the previously measured stellar LSR velocity of  $v_{\text{LSR}} = -23$  km s<sup>-1</sup> (refs. 21, 46) and will be discussed in more detail in the following sections.

**AGB angular diameter.** We took the calibrated data for all ALMA configurations combined, excluding channels with line emission, and fit a uniform disk to the visibilities (as in ref. 54). This gave a diameter of 16.6 mas, containing 8.0 mJy. There was negligible ellipticity or displacement of the centroid. At millimetre wavelengths, a uniform disk is expected to be a better representation of stellar brightness distribution than a Gaussian distribution. The SNR is  $>100$ , suggesting submilliarcsecond precision, based on the nominal uncertainty of beam size divided by SNR, but taking into account possible irregularities in the stellar disk, we adopt a conservative uncertainty of 3 mas. The diameter of  $16.6 \pm 3$  mas is the size of the the surface where electron–neutral free–free emission dominates and is optically thick (at these wavelengths<sup>55</sup>) and corresponds to a radius of  $3.3 \pm 0.6$  au at our adopted distance. We note that the resolution of the continuum image from the extended array is  $21 \times 24$  mas (ref. 50), while for the combined continuum image it is  $40 \times 33$  mas. The optical diameter is  $11.6 \pm 1.8$  mas (ref. 25), 34% smaller than our value. A previous study<sup>55</sup> found that the millimetre-wave diameters of a small sample of AGB stars were 15–50% greater than the optical diameters, consistent with our finding. It has also been found that, in general, the millimetre-wave diameters of the ATOMIUM sample are 30–100% larger than the optical diameters<sup>56</sup>.

**SiN and SiC.** The SiN line we observe towards W Aql ( $N, J = 6, 13/2 \rightarrow 5, 11/2$ ) is a blend of three closely spaced hyperfine components separated by about 0.8 MHz and 0.5 MHz (Supplementary Fig. 1), and the frequency of the centroid is 262,155.78 MHz. The lower spin-rotation component ( $N, J = 6, 11/2 \rightarrow 5, 9/2$ ) at 262.650 GHz falls just outside of the frequency range covered by our observations. The SiC line detected towards W Aql corresponds to the  $J = 6 \rightarrow 5$  transition in the lowest fine-structure ladder  $^3\Pi_2$  (ref. 57). The corresponding  $J = 6 \rightarrow 5$  rotational transitions in the  $^3\Pi_1$  and  $^3\Pi_0$  upper fine-structure ladders fell between the frequency bands covered by our observations.

Neither SiN nor SiC were detected for any other stars in the ATOMIUM sample, all of which are oxygen-rich aside from one other S-type AGB star ( $\pi^1$  Gru). SiC has been previously detected towards 12 carbon-rich AGB stars<sup>58</sup>, but we found no studies of SiC in the envelope of an S-type AGB star. SiN has been previously detected towards W Aql<sup>46</sup> and only one other star: the nearby carbon-rich AGB star CW Leo<sup>26</sup>, which is suspected to have a companion<sup>59–61</sup>. Spatially resolved submillimetre array observations towards CW Leo show the SiN mainly distributed in a shell-like pattern, with some brighter, asymmetric, emission to the southwest<sup>62</sup>. However, a detailed analysis of these observations has not yet been published and, consequently, we lack

detailed spatial information for SiN around other stars with which to compare our W Aql results. Spatially resolved SiC emission has also been observed towards CW Leo, for which SiC was not detected in the innermost regions of the CSE but rather in outer shells<sup>63</sup>, possibly also showing some asymmetry to the southwest<sup>62</sup>. Further discussion of SiC distributions is given in ‘SiN and SiC’ in the ‘Chemical modelling’ section below).

The integrated intensity maps of SiN (Fig. 1a) and SiC (Extended Data Fig. 2a) show emission primarily north and east of the AGB star. The SiN emission has a higher SNR and is hence more readily analysed. Therefore, we have focused our analysis on SiN, but note that the SiC observations agree with the conclusions drawn from SiN.

We produced a series of position–velocity diagrams of SiN using a wide slit (total width 3′) to encompass all the emission seen in the zeroth-moment map (Fig. 1a). Using a narrower slit (such as 0.3′) resulted in a lower SNR in the position–velocity diagram, making an analysis more troublesome. We tested all possible slit angles passing through the position of the AGB star in increments of 5° and then 1° around the angles producing the most distinct position–velocity diagrams. The final slit position of 33° east of north was chosen on the basis of the clarity and intensity of the associated position–velocity diagram. Even though the slit angle was determined independently, we find that it passes through the present position of the F9 star (Fig. 1a). As shown in Fig. 1b, the position–velocity diagram of SiN shows an arc-like structure in position–velocity space, tracing a little more than half an ellipse centred on the AGB star. We fit a parabola to the points in the position–velocity diagram with intensities  $\geq 3\sigma$  above the noise, weighted by the flux at those points. The peak of the parabola, plotted in white in Fig. 1b, is at  $-24.1 \text{ km s}^{-1}$ , which is in agreement with the central velocity we find for the spectral line (Table 1). The emission distribution in the position–velocity diagram does not precisely follow the shape of the parabola, particularly at the negative offset and extreme velocity edges of the emission, so we also plot a partial ellipse based on the position of the parabola (using the centre and peak of the parabola and with the half-width along the velocity axis set to  $14 \text{ km s}^{-1}$ ), which better follows the shape of the emission at the most extreme velocities. We followed a similar procedure for SiC to produce a position–velocity diagram and fit a parabola to the arc of emission (Extended Data Fig. 2b). For SiC, the peak of the parabola is at  $-23.5 \text{ km s}^{-1}$ . We similarly plot a partial ellipse based on the parabola fit (velocity half-width  $13 \text{ km s}^{-1}$ ), which also follows the emission at the most extreme velocities more closely.

In concert, the zeroth-moment map and the position–velocity diagram show that the SiN emission forms an arc to one side of the system, which is close to edge-on or perpendicular to the plane of the sky. We also plot the summed blue and red channels of SiN separately in Supplementary Fig. 3. Owing to the noisy edges of the contours, we could not conclusively determine whether there is an offset between them along the axis connecting the present positions of the AGB and F9 stars. Consequently, we take the orbital inclination of the system to be  $i = 90 \pm 7^\circ$ , where the uncertainty is derived from the beam size. The lack of spherical symmetry in the SiN emission suggests a spatial dependence for the formation of SiN, as discussed in ‘Chemical modelling’ below and depicted in Extended Data Fig. 1. Despite the lower SNR of the SiC emission, the similar structure seen in the position–velocity diagram for SiC indicates a similar formation history for both SiN and SiC.

**NS.** Two rotational transitions of NS were covered by the ATOMIUM observations—the  $J = 11/2 \rightarrow 9/2$  hyperfine split multiplets in the  $^2\Pi_{1/2}$  and  $^2\Pi_{3/2}$  spin–orbit fine-structure components. Neither rotational transition was detected in spectra centred on the AGB star. However guided by predictions from chemical models (see ‘NS’ in ‘Chemical modelling’ below and ref. 4), we conducted a more careful search for NS. The transition in the ground  $^2\Pi_{1/2}$  component lies very close to the edge of our frequency band and is difficult to discern in the spectra, but

we successfully detected it in the zeroth-moment map (Extended Data Fig. 3a). The corresponding rotational transition in the upper ( $^2\Pi_{3/2}$ ) spin–orbit component at 255.597 GHz (ref. 64) lies about 322 K above the ground state and is estimated to be about three times less intense. We found an upper limit for the  $^2\Pi_{3/2}$  component of  $3\sigma = 0.047 \text{ Jy per beam km s}^{-1}$  in a zeroth-moment map that covers the same velocity extent as that observed for the ground  $^2\Pi_{1/2}$  component.

Before this, NS had been detected towards just one AGB star, the oxygen-rich IK Tau<sup>65,66</sup> (and notably has not been detected towards the nearby carbon star CW Leo). An enhanced abundance of NS is expected to be a good tracer of binarity for S-type or oxygen-rich AGB stars with main-sequence or white-dwarf companions<sup>4</sup>. We checked the ATOMIUM data for NS detections towards other sources. While we could rule out NS detections in several sources, for a selection of others (the AGB stars IRC+10011 and IRC–10529, and the red supergiants VX Sgr and AH Sco) we could not conclusively confirm or rule out the presence of NS for three reasons. First, the  $^2\Pi_{1/2}$  component at 253.968 GHz lies close to the edge of an observed band in frequency space, meaning that the line may be partially truncated, as it is for W Aql. Second, that line lies close to the  $\text{SO}_2$  ( $J_{K_a, K_c} = 15_{6,10} \rightarrow 16_{5,11}$ ) line at 253.957 GHz (where the quantum number  $K_a$  refers to the projection of the total angular momentum,  $J$ , along the axis of the least moment of inertia,  $a$ , and  $K_c$  refers to the projection of  $J$  along the axis of the largest moment of inertia,  $c$ ) and, for the oxygen-rich sources mentioned above, we cannot easily disentangle which emission comes from  $\text{SO}_2$  and which might come from NS. (This is not a problem for W Aql, towards which no  $\text{SO}_2$  lines are detected, including more intrinsically intense lines covered by our observations.) Disentangling NS and  $\text{SO}_2$  emission is made more difficult because both lines are truncated by the edge of the observed band. Finally, we also checked for emission from the  $^2\Pi_{3/2}$  component at 255.597 GHz but could not confirm the detection of this line of NS. For the AGB stars mentioned above, we did not detect emission above the noise of our observations. However, if we take the expected intensity of the  $^2\Pi_{3/2}$  component to be a third that of the truncated and possibly blended line around 253.968 GHz, we determine that the expected intensity is below the noise of our observations. For the two red supergiants, the potential NS line is blended with a high-energy  $\text{SO}_2$  line, ( $J_{K_a, K_c} = 51_{7,45} \rightarrow 50_{8,42}$ ) at 255.595 GHz. Therefore, to determine whether NS is present in these or other ATOMIUM stars, observations of other NS transitions that do not overlap with  $\text{SO}_2$  or other molecular lines are required.

In addition to the zeroth-moment map, we also constructed a position–velocity diagram of NS (Extended Data Fig. 3b). The only significant region of emission that is  $3\sigma$  above the noise in the position–velocity diagram is located on the red side of the diagram and not notably offset from the position of the AGB star. This is close to some of the most intense regions seen in the SiN and SiC position–velocity diagrams. We note that because the NS line is on the edge of the observed band, some redder emission might not have been recovered by our observations. To emphasize that this is a true detection of NS rather than a misidentified line, we plot the spectrum of the NS line with the spectra of the SiN and SiC lines in Extended Data Fig. 3c. All lines were extracted from circular apertures with radii 0.25′, centred on the continuum peak, which was chosen to best show the NS line. All three lines have a double-peaked profile, with SiN and NS having a brighter red peak than blue peak. Although the NS spectrum is truncated at  $-9 \text{ km s}^{-1}$ , it can be seen rising in a profile similar to the SiN and SiC red peaks. Deeper observations targeting NS would confirm this behaviour.

**HC<sub>3</sub>N.** Four successive rotational lines of HC<sub>3</sub>N were detected towards W Aql as part of the ATOMIUM project (Table 1). Before this, the three lowest transitions in this group were tentatively detected towards W Aql with APEX<sup>46</sup>. A comparison of the lines tentatively detected with APEX and our ALMA data suggests that the ALMA data do not suffer from resolved-out flux. It should also be noted that the  $J = 25 \rightarrow 24$

and  $J = 27 \rightarrow 26$  lines were observed with all three ALMA configurations (including the compact configuration), while the  $J = 26 \rightarrow 25$  and  $J = 28 \rightarrow 27$  lines were observed with only the extended and medium configurations. All four lines have similar intensities when the spectra are extracted from our combined data cubes, as expected for lines with similar energies (the lower-level energies span 131–165 K) and Einstein  $A$  coefficients. Taken together, our observations confirm that there is no flux resolved out for the observations with the medium configuration. Most of the  $\text{HC}_3\text{N}$  flux is located south and west of the present location of the AGB star (Fig. 4 and Extended Data Fig. 6), in direct contrast to the observed flux of SiN and SiC (Fig. 1 and Extended Data Fig. 2).

**CO.** The  $\text{CO } J = 2 \rightarrow 1$  line has the most extended emission distribution of all the spectral lines observed towards W Aql as part of the ATOMIUM programme. Although only one-third of the flux was recovered by ALMA (see ‘Data reduction’ above), our analysis focuses on smaller structures in the wind, which are not affected by resolved-out flux.

Many complex structures are seen in the CO emission, making a definitive analysis difficult. We first examined the inner wind region, where an overdensity thought to be (part of) a spiral arm was reported<sup>23</sup>. In this region, we found an approximately circular structure that corresponds very well to the location of the overdensity and to the radius of the observed SiN emission. In Fig. 5b, we plot the CO emission close to the AGB star using a logarithmic colour scale and overplot the contours of SiN (as seen in Fig. 1a) and a black circle to guide the eye to the roughly circular structure. The radius of this circle is 1.35'' and its centre is 0.1'' to the north of the AGB star.

Additional circular structures in the CO emission were more difficult to concretely identify, so we plotted the radial intensity against anticlockwise angle to help find such structures (Extended Data Fig. 8). Circular structures centred on the AGB star would appear as horizontal lines in such a plot, whereas off-centre circular structures appear as sinusoids. Using the angle–radius plot, we found off-centre circles corresponding to: red, the edge of the bright central region with a radius of 4''; pink, a circular structure surrounding this region, with a radius of 5.5''; and white, another circle with radius 10.75'' that falls close to the edge of the ALMA field of view. The white circle is offset in the same direction (north) as the black circle. Note that the sinusoid corresponding to the black circle identified above can be seen more clearly in the angle–radius plot when it is zoomed in on the structures closer to the AGB star (Extended Data Fig. 8, bottom). In Supplementary Fig. 4 we show the same angle–radius plots as in Extended Data Fig. 8, but exclude the coloured lines highlighting the aforementioned structures.

We plot all these circular structures in Fig. 5a over the averaged central three channels of the CO emission. From our analysis with the hydrodynamic model (see ‘Hydrodynamic simulations’) we come to the conclusion that the black and white circles were formed during the periastron passage of the two stars, in which case they are expected to be offset to the opposite side of the AGB star from the F9 star. The periastron origin of the black circle is also supported by its co-location with the SiN arc. The red and pink circles, and other irregular structures, are not directly reproduced by the hydrodynamic model, but this is probably because of limitations in the model, including missing physics around pulsations and the wind launching mechanism (see discussion in ‘Hydrodynamic simulations’). Significantly, the wind is launched at  $13 \text{ km s}^{-1}$  in the hydrodynamic model, whereas previous studies assume a much lower initial velocity of  $3 \text{ km s}^{-1}$ , close to the sound speed. This discrepancy prevents a dense inner region forming in the hydrodynamic model, such as the region encircled in red in Fig. 5a. We also note that the formation timescales of the red and pink circles and other neighbouring features are  $\lesssim 300$  years (taking  $\beta$ -law wind acceleration into account) and do not match the longer timescale of the binary orbit inferred from resolved imaging (see ‘Spatially resolved imaging’).

When comparing these circular structures with the lower-resolution ( $0.47 \times 0.41$ ) ALMA observations of CO ( $3 \rightarrow 2$ ) around

W Aql<sup>22</sup>, in which several circular arcs were identified, we find that our red, pink and white circles correspond to the locations of those arcs. In particular, the outermost arc in the earlier data corresponds well with our white circle, and the innermost two arcs (north and southwest) match the position of our red circle. The circular region of higher flux that we have indicated in red in Fig. 5a for CO ( $2 \rightarrow 1$ ) also corresponds to the region of higher flux seen in CO ( $3 \rightarrow 2$ ). The remaining arcs identified by ref. 22 match our pink circle and a few other structures seen in our data that do not form full circles. Note that our black circle is too small to be well resolved in the earlier data.

The shell-like structures seen around W Aql have some similarity to previously reported shells around the carbon star CW Leo, which are also not perfectly centred on the AGB star<sup>59,68</sup>. Many more shells are seen for CW Leo than W Aql, probably in part because CW Leo is closer, making emission easier to detect. Studies of the CW Leo shells have concluded that they could be caused by an eccentric binary orbit seen perpendicular to the line of sight, and assumed some periods of enhanced mass loss<sup>59,68</sup>. Our hydrodynamic models do not assume a variable mass-loss rate (see ‘Hydrodynamic simulations’) but still form shell-like structures when viewed perpendicular to the orbital plane. This does not mean that the mass-loss rate of W Aql cannot be variable—indeed variable or anisotropic mass-loss might account for some of the other structures seen in the CO emission. The possible effects of variable and anisotropic mass loss are discussed in more detail in ‘Anisotropic mass loss’ in Supplementary Information.

We also analysed the higher- and lower-velocity channels of the W Aql CO emission, particularly in comparison with the hydrodynamic model. A long-standing unexplained phenomenon is excess emission in the blue wings of the line profiles of CO and other molecules towards W Aql<sup>21</sup>. In our ALMA observations of CO (Extended Data Fig. 7), it is clear that the blue- and redshifted channel maps are not symmetric around the LSR velocity. The blue channels ( $-37 \text{ km s}^{-1}$  to  $-30 \text{ km s}^{-1}$ ) show slightly asymmetric emission, with an elongation in the southwest direction, while the red channels ( $-14 \text{ km s}^{-1}$  to  $-8 \text{ km s}^{-1}$ ) show emission with more circular symmetry. These differences in shape account for the excess emission in the blue wing of the line profiles. We also compared these different emission distributions with the equivalent distributions produced by the hydrodynamic model after processing by the radiative transfer code MCFOST (see ‘Hydrodynamic simulations’). In Extended Data Fig. 9, we plot two CO channels equidistant from the LSR velocity and the equivalent model channels. The model also shows the elongated CO emission for the blue channel and the more circular emission for the red channel, reinforcing that the asymmetry arises from the companion’s interactions with the AGB wind.

**Other molecular species.** The species SiO, SiS, HCN and CS are commonly observed in the envelopes of many AGB stars of all chemical types<sup>37,69–71</sup>. All four molecules were observed previously towards W Aql at a lower spatial resolution of  $0.55'' \times 0.48''$  (ref. 23) and were analysed using radiative transfer models under the assumption of spherical symmetry. Our observations were obtained at a much higher angular resolution and the emitting regions for all four molecules are very well resolved (Table 1 and Fig. 3). The increased angular resolution allows us to observe asymmetries in the emission. The emission from all four molecules is more extended to the northeast than to the southwest. This is a qualitatively similar anisotropy to that seen in SiN, but unlike SiN, the more common species show roughly spherically symmetric emission across a much wider fan-like region, running clockwise from east to northwest (Fig. 3). In the context of an eccentric binary companion, we interpret this not as enhanced production of SiO, SiS, HCN and CS triggered during the periastron passage (as we conclude in the cases of SiN and SiC), but as enhanced destruction through photodissociation of SiO, SiS, HCN and CS by the F9 companion, during the large portion of the orbital period it spends to the southwest of the AGB star. If this were not the case, we should see significantly less emission to the

northwest and southeast (that is, the other regions where we do not see SiN), but the contours in Fig. 3 have similar extents from the southeast to northeast to northwest. This is especially apparent in plots of the central channels of SiS and CS, shown in Extended Data Fig. 4, which show significantly reduced emission near the F9 star as opposed to on the opposite side of the AGB star. For CS, the  $3\sigma$  contour centred on the AGB stars extends out to  $0.33''$  ( $-2 \times 10^{15}$  cm) from the AGB star in the direction of the F9 star, compared with  $0.71''$  ( $-4 \times 10^{15}$  cm) in the opposite direction. For SiS, the  $3\sigma$  contour centred on the AGB star extends out to  $0.09''$  ( $-5 \times 10^{14}$  cm) in the direction of the F9 star and out to  $0.23''$  ( $-1 \times 10^{15}$  cm) in the opposite direction.

Furthermore, the position–velocity diagrams of CS, SiO and H<sup>13</sup>CN, taken along the same axis as we used for SiN and plotted in Supplementary Fig. 5, show the brightest emission spatially close to the AGB star, not in an arc as for SiN or SiC. They also show that the emission is consistently less extended and less intense on the side of the AGB star where the F9 star is located. Notably, this is not the case for CO, also plotted in Supplementary Fig. 5, which does not show evidence of photodissociation by the F9 star, as expected given its stronger bond energy and self-shielding<sup>72</sup>. The reduced emission seen in the spectra around the F9 star (see ‘Molecular emission around F9 star’ below) is further evidence of most molecules being destroyed by the F9 flux.

Another molecular species that shows highly asymmetric emission around W Aql is <sup>13</sup>CN. Although the main isotopic species, <sup>12</sup>CN, was not covered in the ATOMIUM observations, it has previously been observed towards W Aql with the Institut de Radioastronomie Millimétrique (IRAM) 30 m telescope<sup>73</sup>. We find that, unlike the common molecular species discussed above, the <sup>13</sup>CN emission is mainly seen on the opposite side of the AGB star. As can be seen from the zeroth-moment maps of H<sup>13</sup>CN and <sup>13</sup>CN in Fig. 4, the <sup>13</sup>CN emission is mainly observed where the H<sup>13</sup>CN emission is absent, which is consistent with the generally accepted notion that CN is a photodissociation product of HCN<sup>27</sup>. This is discussed in more detail in ‘Chemical modelling’.

**Molecular emission around F9 star.** We extracted spectra in circular apertures of radii 100 mas (corresponding to a projected radius of 40 au) centred on the F9 star to check for anomalous emission. Very few lines were detected above the noise in these spectra, with lines originating only from CO, SiO, CS and HCN. We compared the line profiles extracted from the region around the line-of-sight position of the F9 star with profiles of the same size aperture centred on the AGB star and plot comparisons for CS, HCN and SiO in Extended Data Fig. 5. Notably, the F9-centred line profiles show relatively more flux in the blue channels and less flux in the red channels than the corresponding AGB-centred profiles. The F9-centred profiles also tend to have relatively less emission in the channels close to the LSR velocity. From this, we can estimate that the F9 star is located, spatially, in the region that corresponds to gas with velocities close to the AGB stellar LSR velocity, that is, gas with motions approximately in the plane of the sky. This estimate is possible because, in an expanding CSE, the velocity axis has a correspondence to the line-of-sight spatial axis (see, for example, ref. 68). Although this does not say anything about the present velocity of the F9 star (it need not be moving at the same velocity as the AGB circumstellar gas that it is moving through), it is consistent with the stars being in a highly eccentric orbit, as the present relative motion of the F9 star would be predominantly in the plane of the sky rather than into or out of the plane of the sky, and would, in any case, have a low absolute total velocity of  $\sim 2$  km s<sup>-1</sup>.

We also checked the shape of the line profiles extracted for an equivalent 100 mas aperture on the opposite side of the AGB star from the F9 star (at the same projected separation) and found that those line profiles were more similar to the AGB-centred line profiles than those centred on the F9 star (Extended Data Fig. 5). Finally, we note that the phenomenon of the blue peaks being brighter than the red peaks for the F9-centred profiles is the opposite of what we see for the line profiles

of SiN and NS (Extended Data Fig. 3c) centred on the AGB star. This is easily explained by the different formation/destruction times of the two groups of molecules: SiN and NS formed during the periastron passage, whereas CS, HCN and SiO are currently being (partly) photodissociated by the UV flux of the F9 star.

The intensity of the UV flux from the F9 star is proportional to the inverse square of the distance from the star. This means that the apparent UV flux close to the AGB star, taking the projected separation of 194 au, is 24 times less than the flux 40 au from the F9 star, and the flux on the opposite side of the AGB star (at a distance of 388 au) is 94 times weaker. At a distance of 10 au from the F9 star, close to the distance between the two stars during periastron, the UV flux would be 380 times higher than the flux on the same region at the present stellar separation. Note that these values are rough estimates and do not include, for example, UV extinction by dust, which would further reduce the UV flux for larger distances when there is more dust between the F9 star and the region of interest.

### Radiative transfer modelling

Radiative transfer calculations were undertaken to approximate the abundance of SiN in the arc seen in Fig. 1. To achieve this, we extracted the SiN spectra from round apertures with radii of  $0.25''$ , evenly spaced with centres separated by  $0.3''$  starting from the continuum peak and moving outwards along the north  $33^\circ$  east line passing through the emission. The set-up is shown in Supplementary Fig. 6a, where the regions are labelled from A to H. The aperture size was chosen to not lie outside of the detected SiN emission. Furthermore, these regions are centred along the same axis for which we found the best PV diagram (Fig. 1b and ‘ALMA results’), so they are unlikely to overlap with the edges of the SiN emission. Therefore, by considering only spectra from the regions plotted in Supplementary Fig. 6c, we can use a one-dimensional (spherically symmetric) radiative transfer model to compare equivalent synthetic spectra and determine the SiN abundance distribution in the arc, which can also be approximated by a wedge of a spherical shell. Our approach is viable because the SiN emission is expected to be optically thin (and indeed we find a peak tangential optical depth of  $\tau \lesssim 0.2$  in the model) and emission in other parts of the spherically symmetric model (at different velocities) is not expected to interact with emission in the regions of interest.

We used the accelerated lambda iteration method (ALI<sup>74</sup>), which has been previously used to determine the abundances of various other molecules in the CSE of W Aql<sup>23,24</sup>. We use previously determined circumstellar parameters for W Aql<sup>21</sup>, including a radial temperature profile, the mass-loss rate of  $3 \times 10^{-6} M_\odot \text{ yr}^{-1}$  (ref. 22) and a velocity profile described by ref. 21

$$v(r) = v_0 + (v_\infty - v_0) \left(1 - \frac{R_{\text{in}}}{r}\right)^\beta \quad (2)$$

with  $v_0 = 3$  km s<sup>-1</sup> the velocity at the dust condensation radius,  $R_{\text{in}} = 2 \times 10^{14}$  cm,  $v_\infty = 16.5$  km s<sup>-1</sup> the terminal expansion velocity and  $\beta = 2$ . The key stellar and circumstellar parameters are summarized in Supplementary Table 1. We also included a previously implemented overdensity<sup>23</sup>, which was found to improve the radiative transfer model fit for ALMA observations of CS and H<sup>13</sup>CN at lower resolutions<sup>23</sup>. The overdensity relates to an increase in the H<sub>2</sub> number density by a factor of five between the radii of  $8 \times 10^{15}$  cm and  $1.5 \times 10^{16}$  cm (Supplementary Fig. 6), and is in good agreement with the location of a region of increased CO emission (a good tracer of density) traced by the black circle in Fig. 5b. (Previously the overdensity was thought to be part of an unresolved spiral arm<sup>23</sup>.)

We include SiN energy levels up to  $N = 20$  in the ground vibrational state and the 59 radiative transitions connecting those levels. The energy levels and Einstein *A* coefficients were calculated using CALPGM<sup>75</sup> and take fine structure into account but neglect the closely

spaced hyperfine structure, which is not resolved in our observations. There are no calculated or measured collisional (de)excitation rates for SiN, so instead we use the rates calculated for CN–He (ref. 76), scaled by 1.37 to account for the different reduced mass of the SiN–H<sub>2</sub> system.

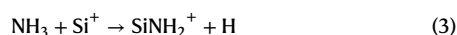
On the basis that the different extraction apertures shown in Supplementary Fig. 6a probe different regions of the SiN distribution, we tried various shapes for the radial distribution of SiN abundance in an attempt to reproduce the observed distribution of SiN. These included a constant abundance, step functions of different constant SiN abundances, and Gaussian shells of various widths and positions. We also left the inner and outer radii of the SiN-emitting region as free parameters. We found that while the two apertures farthest from the continuum peak, G and H, were sensitive to the outer radius and outer abundance of the SiN distribution, as expected, the inner apertures, A to D, were also sensitive to these properties, which affected the heights of the emission peaks in their double-peaked profiles. Conversely, the choice of inner radius and the innermost abundance of SiN mainly affected the heights of the line centres for apertures A to C. These dependencies were expected given the observed wedge of SiN emission.

Our best-fitting model has a constant outer SiN abundance relative to H<sub>2</sub> of  $1.5 \times 10^{-7}$ , from  $6 \times 10^{15}$  cm to  $2 \times 10^{16}$  cm, and a power-law distribution in the inner part, starting from an inner radius of  $1.5 \times 10^{15}$  cm. This distribution is plotted in Supplementary Fig. 6b, where we also show the H<sub>2</sub> number density over the same region, including the aforementioned overdensity. As can be seen from Supplementary Fig. 6b, the extended peak of the SiN abundance spans the region of the H<sub>2</sub> overdensity. This further supports the idea that both phenomena have a common cause, which we postulate is the periastron passage of the AGB and F9 stars. The line profiles generated by the best-fitting models are plotted with the spectra in Supplementary Fig. 6c.

### Chemical modelling

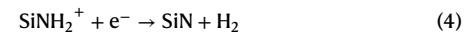
The recent results of ref. 4 focus on the effect of close companions on the circumstellar chemistry. In Supplementary Fig. 7, we reproduce their results for stars with similar wind density to W Aql (model  $\dot{M}/v_{\infty} = 2 \times 10^{-6} M_{\odot} \text{ yr}^{-1}/(\text{km s}^{-1})$ ) compared with W Aql ( $\dot{M}/v_{\infty} = 1.8 \times 10^{-6} M_{\odot} \text{ yr}^{-1}/(\text{km s}^{-1})$ ), showing the predicted abundances of SiN, SiC and NS for both oxygen- and carbon-rich outflows, with and without an F9-like companion. The companion is approximated by a black body at 6,000 K and does not explicitly include chromospheric UV photons. However, observations of W Aql with the Galaxy Evolution Explorer (GALEX) in 2006 reveal a detection in the near UV (22.16 mag, 1,771–2,831 Å) but not in the far UV (>22.5 mag, 1,344–1,786 Å)<sup>77</sup>, the latter being more important for breaking molecular bonds. If additional chromospheric UV flux is generated around periastron, as has been suggested for other types of star in close binary systems<sup>78,79</sup>, then this would mainly serve to increase the products of UV photochemistry, such as Si<sup>+</sup>, which are discussed below. An excessively large UV excess during periastron could possibly destroy a larger variety of molecular species than predicted, but this would occur over a relatively short timescale (Extended Data Table 1 and ‘Orbital solutions’) and would not preclude further chemical interactions, including many of the formation channels discussed below, once the stars moved further apart.

**SiN and SiC.** The chemical models<sup>4</sup> show that, in the absence of a companion, the SiN radical is expected to form in a shell-like distribution, with a peak abundance at a radius of around  $10^{16}$  cm from the AGB star (Supplementary Fig. 7). The main formation pathway of SiN is via the measured reaction



where NH<sub>3</sub> is assumed to be a parent species that is formed close to the AGB star and, through observations, has been found to have a

peak abundance of  $\sim 2 \times 10^{-5}$  relative to H<sub>2</sub> (ref. 21). This is followed by dissociative recombination



The main source of Si<sup>+</sup> is the photodissociation of SiS, that is



which occurs very readily in the presence of the F9 companion (Supplementary Fig. 8) and the UV photons it emits<sup>4</sup>; and is confirmed in our observations (Fig. 3 and Extended Data Fig. 4), because SiS is noticeably depleted to the southwest at the present position of the F9 star. We also note that there are minor formation pathways for SiN forming from HNSi and SiC, but both pathways also depend on NH<sub>3</sub> and Si<sup>+</sup> and hence are also affected by UV photons driving the formation of Si<sup>+</sup>.

In the chemical models<sup>4</sup> (Supplementary Fig. 7), the main difference in the SiN abundance distributions between oxygen- and carbon-rich stars with the same wind density and no companion is that the peak relative abundance of SiN is predicted to be  $\sim 10^{-8}$  for the oxygen-rich star and  $\sim 10^{-7}$  for the carbon-rich star. W Aql is an S-type star whose chemistry is presumed to be intermediate between the typical carbon-rich and oxygen-rich stars<sup>21</sup>, and that is what has been found for the abundances of HCN in S-type stars<sup>69</sup>. However, we find that the peak abundance of SiN in W Aql ( $1.5 \times 10^{-7}$  relative to H<sub>2</sub>, see ‘Radiative transfer modelling’ above) is in good agreement with that predicted for a carbon-rich star, although the asymmetric distribution of SiN implies that the formation process is anisotropic.

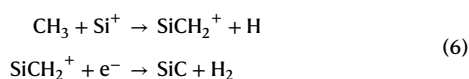
Reference<sup>4</sup> focused on the impact of UV photons from stellar companions on the circumstellar chemistry of AGB stars. It included a set of models with a main-sequence companion with a stellar effective temperature of 6,000 K that is comparable to the temperature of an F9 dwarf<sup>80</sup> (reproduced in Supplementary Fig. 7). The radial abundance profile of SiN is significantly altered by the companion—that is, the peak abundance of SiN in both the carbon- and oxygen-rich winds is higher, and the abundance of SiN in the inner part of the wind is also higher. For the oxygen-rich outflow, the inner abundance of SiN is higher at  $\sim 10^{-7}$ , and it remains relatively constant until it begins to decrease at around  $10^{16}$  cm; SiN does not show a shell-like distribution, as it would in the absence of a companion, but rather a parent-like distribution with a high inner abundance followed by a Gaussian decline caused by photodissociation driven by the interstellar radiation field. For the carbon-rich outflow, a shell-like distribution is seen in the presence of the companion, but the peak abundance is higher ( $\sim 10^{-6}$ ) and the inner abundance of SiN is several orders of magnitude higher ( $\sim 2 \times 10^{-9}$  relative to H<sub>2</sub>), than it would be if the companion were not present. An underlying assumption in these models is that the companion star is always close to the AGB star<sup>4</sup>. However, this is not the case for W Aql, as the projected distance between the F9 and AGB stars is presently 194 au or  $2.9 \times 10^{15}$  cm, rather than  $2\text{--}5 R_{\star}$  ( $4 \times 10^{13}\text{--}10 \times 10^{13}$  cm) as assumed in the chemical models<sup>4</sup>. A highly elliptical orbit, during which the F9 star passes within a few stellar radii of the AGB star, could result in the asymmetric emission by SiN that we see in Fig. 1, if the F9 star only drove the production of SiN while it was sufficiently close to the AGB star. In this instance, the temporary close proximity of the two stars is relevant, because the wind region close to the AGB star is the densest and the chemical reactions will occur more readily. For example, at 5 au from the AGB star, the H<sub>2</sub> number density is  $3 \times 10^9 \text{ cm}^{-3}$ , whereas at the current projected distance of the F9 star, the number density is four orders of magnitude smaller, at  $3 \times 10^5 \text{ cm}^{-3}$ . Because the rates of chemical reactions generally depend on (the square of the) number density, a lower number density results in a corresponding decrease in reaction rates, and hence much lower SiN production. Even very fast periastron interactions (Extended Data Table 1) are still long enough

to produce SiN, particularly as, for example, the photoionization of Si to Si<sup>+</sup> (equation (5)) proceeds very quickly in the presence of the companion.

Once formed, we expect SiN to persist in the expanding CSE until it is photodissociated by the interstellar radiation field, based on chemical modelling<sup>4</sup> and because it is not expected to participate in the formation of dust or other molecular species. In general, the photodestruction timescale of a molecule being dissociated by the interstellar radiation field depends on the photodissociation rate for that molecule and on the extinction, with higher extinctions meaning that fewer photons will penetrate to that region. This is taken into account in the chemical models and accounts for the drop off in abundance in the outer regions of the CSE (Supplementary Fig. 7), which, for SiN, agrees with the location of the drop off we found from radiative transfer modelling (see ‘Radiative transfer modelling’). The additional UV photons originating from the F9 star have only a relatively local effect on the chemistry of the CSE; as discussed in ‘Other molecular species’ and ‘Molecular emission around F9 star’ in ‘ALMA results’ and shown in Fig. 3 and Extended Data Fig. 5, the F9 star contributes to photodissociation of molecules in its vicinity, but not on the opposite side of the CSE.

SiC behaves in a broadly similar way to SiN in the chemical models, with and without the inclusion of a main-sequence companion<sup>4</sup> (Supplementary Fig. 7, middle). For both carbon- and oxygen-rich CSEs without a companion, SiC is expected to be distributed in a shell around the star, albeit with a more shallow gradient on either side of the peak than for SiN. For the carbon-rich star with a density similar to W Aql, the peak abundance of SiC is located at  $-10^{16}$  cm from the AGB star and is found to be  $-10^{-6}$  relative to H<sub>2</sub>, while for the oxygen-rich CSE, the peak of  $-5 \times 10^{-9}$  is found slightly farther from the star at  $-3 \times 10^{16}$  cm. The presence of an F9-like companion alters the SiC distribution in a similar way as for SiN, changing it from a shell-like distribution to a more centralized distribution. The abundance in the inner part of the distribution (that is, in the region from the inner edge of the model to  $-10^{16}$  cm) increases up to  $-2 \times 10^{-5}$  for the carbon-rich CSE; and  $-5 \times 10^{-9}$  for the oxygen-rich CSE, where there is previously negligible SiC in this region without a companion (Supplementary Fig. 7).

Analogous to SiN (equations (3) and (4)), SiC mainly forms via



with the same source of Si<sup>+</sup> as explained in equation (5). CH<sub>3</sub> is formed either via photodissociation of CH<sub>4</sub> or through the successive hydrogenation of C. The former pathway is dominant for carbon-rich CSEs, while the latter is more likely in oxygen-rich CSEs. For an S-type star such as W Aql, both pathways may contribute to CH<sub>3</sub> formation.

The formation of both SiN and SiC is driven by Si<sup>+</sup>, which forms through the photoionization of Si (equation (5)). In Supplementary Fig. 8, we plot the predicted abundances of Si<sup>+</sup> with and without the presence of the F9 companion<sup>4</sup>. While the abundance of Si<sup>+</sup> naturally rises in the outer part of the envelope (beyond  $-10^{16}$  cm), owing to the interstellar radiation field, the inner abundance rises significantly in the presence of an F9-like companion. We note that although the abundance of Si<sup>+</sup> rises to  $10^{-9}$  to  $10^{-7}$ , for oxygen- and carbon-rich CSEs, respectively, this is still significantly less than the total abundance of Si ( $6.5 \times 10^{-3}$  relative to H<sub>2</sub>, assuming solar elemental abundances<sup>81</sup>), meaning that the photoionization process driven by the F9 star is not expected to ionize all the Si.

**NS.** In the absence of a companion, NS is expected to form in a shell with a peak at about  $10^{16}$  cm (ref. 4). For a carbon-rich CSE, the addition of an F9 companion does not cause a significant difference in the NS distribution. For an oxygen-rich CSE, however, the chemical model with an F9-like companion predicts a higher abundance of NS by almost an order of magnitude and significantly changes the shape of

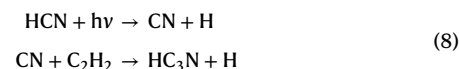
the distribution, resulting in a high abundance of NS in the inner wind ( $-10^{-6}$ , which decreases from around  $5 \times 10^{15}$  cm).

NS is formed via the photodissociation of N<sub>2</sub> (ref. 4)



Even though the rate of photodissociation of N<sub>2</sub> is relatively low because of the strong bond, the abundance of N<sub>2</sub> is thought to be high ( $4 \times 10^{-5}$  relative to H<sub>2</sub> (ref. 82)). Therefore, even if only  $\leq 1\%$  of N<sub>2</sub> is destroyed, enough N is liberated to form NS<sup>4</sup>. The predicted abundance distribution of N, taking into account the presence of an F9-like companion, is plotted in Supplementary Fig. 8. The detection of NS is tentative (Extended Data Fig. 3), but its co-location with the brightest region of SiN (especially in the position–velocity diagram; Fig. 1b) and the predictions of chemical models that include an F9-like companion<sup>4</sup> (Supplementary Fig. 7), suggest that NS was probably formed during the periastron passage of the W Aql system, when the F9 star irradiated part of the inner wind.

**HCN, CN and HC<sub>3</sub>N.** HCN, CN and HC<sub>3</sub>N are closely linked species that have a wide astronomical literature in the context of the cyanopolyne (H–(C≡C)<sub>n</sub>–C≡N) family of molecules. HCN is a parent species formed close to the star<sup>82</sup> and CN has long been known to be a photodissociation product of HCN<sup>27</sup>. At low temperatures (below 800 K (ref. 83)), where HC<sub>3</sub>N is seen towards W Aql, the main formation pathway for HC<sub>3</sub>N is from the two parent species HCN and C<sub>2</sub>H<sub>2</sub> (refs. 83,84):



For most molecular species, chemical fractionation of isotopologues is expected to be negligible around AGB stars. Hence, we can use the observations of H<sup>13</sup>CN and <sup>13</sup>CN to understand the formation of H<sup>12</sup>C<sub>3</sub>N. For the rest of this section, we omit the isotope labels. As can be seen in Fig. 4, CN is preferentially detected on the side of the CSE where the F9 star is currently located, coinciding with a region of HCN depletion. We refer to this phenomenon as depletion because it aligns well with the location of the F9 star and of CN, and because the extent of HCN to the northeast agrees well with the predicted extent of HCN in the chemical models, in the absence of a companion<sup>4</sup> (see also discussion in ‘SiO, SiS and CS’ below). Although the F9 star passes close to the AGB star during the eccentric orbit, the amount of time the stars spend close together is relatively short,  $\lesssim 2\%$  of the orbital period (Extended Data Table 1 and ‘Orbital solutions’), compared with the amount of time the F9 star spends to the southwest of the AGB star, providing a relatively consistent source of UV radiation. A similar pattern of molecular depletion is seen for SiO, SiS and CS (Fig. 4) for the same reason.

HC<sub>3</sub>N is present on the same side of the CSE as CN (Fig. 4 and Extended Data Fig. 6), from which we can infer that the presence of CN preferentially drives the formation of HC<sub>3</sub>N to the south and west of the AGB star. Although HC<sub>3</sub>N has long been known to be present around carbon stars, W Aql is the only S-type AGB star towards which HC<sub>3</sub>N has been studied. Although HC<sub>3</sub>N and other carbon-bearing molecules such as C<sub>2</sub>H and SiC<sub>2</sub> seem to indicate a carbon-rich circumstellar chemistry for W Aql<sup>46</sup>, the spectroscopic classification of W Aql marks it as an S-type star<sup>18</sup>. It is possible such carbon-bearing species are common around (some subset of) S-type stars more generally, but, so far, W Aql has been studied in the most detail.

HC<sub>3</sub>N has been most widely studied around the nearby carbon star CW Leo, where it is located mainly in a spherical shell centred on the star, well resolved in ALMA observations and as predicted by chemical models<sup>4,83</sup>, with some enhancement in the inner regions which is thought to be driven by a companion<sup>61</sup>. We do not see a symmetric shell-like distribution of HC<sub>3</sub>N around W Aql (Extended Data Fig. 6);

however, we interpret the HC<sub>3</sub>N that we observe as part of a broken shell that is formed where CN is more abundant.

Although we expect that some CN—and subsequently HC<sub>3</sub>N—would have formed during or as a result of the periastron passage of the W Aql binary, these two molecules will have expanded with the CSE (as SiN has), to a radius that is comparable to the black circle in CO (1.35″; Fig. 5). At this distance from the AGB star, some CN might remain but is not easily detectable above the noise in our observations. Some traces of <sup>13</sup>CN are seen north of the AGB star in Fig. 4, but the SNR of the <sup>13</sup>CN observation is relatively low, partly because more than half of the flux was resolved out (Table 1). We also note that <sup>12</sup>CN, expected to be around 10 to 30 times more abundant<sup>21</sup>, was not covered by our observations. Hence, we cannot conclusively determine how much CN is present to the northeast of the AGB star, relative to the apparently higher abundance of CN to the southwest, closer to the F9 star. More sensitive observations, ideally covering <sup>12</sup>CN and not subject to resolved out flux, would be required to fully understand the distribution of CN around W Aql. We note the CN we expect to be co-located with SiN, which should have formed during the periastron interaction, is harder to detect than SiN is, for several reasons relating to the molecular physics and energy-level distributions of the two molecules. Although SiN is also subject to hyperfine splitting, the three most intense hyperfine components are separated by only ~1.4 MHz, a tiny separation compared with the 30 km s<sup>-1</sup> (22 MHz) width of the SiN line, as can be seen in Supplementary Fig. 1b. In comparison, the spectrally resolved hyperfine splitting of CN results in especially wide lines that have lower peak intensities than they would in the absence of hyperfine splitting. This makes them harder to detect above the noise. Furthermore, the dipole moment of SiN is around 1.8 times larger than for <sup>13</sup>CN (refs. 85,86), resulting in intrinsically brighter lines for SiN.

The excitation conditions of the observed lines of HC<sub>3</sub>N are such that we do not expect to see these same lines of HC<sub>3</sub>N lines farther out in the wind than we do in Fig. 4 (<0.5″). Therefore, if any HC<sub>3</sub>N is present at a radius of 1.35″ from the AGB star, we would not have detected it in the present observations. We predict that HC<sub>3</sub>N in this region could be detected in more sensitive observations covering lower-energy transition lines.

**SiO, SiS and CS.** The emission seen from SiO, SiS and CS (Fig. 3)—like that of HCN—indicates photodissociation driven by the F9 star during its time to the southwest of the AGB star, unlike SiN, SiC and NS whose formation is driven by the brief but intense addition of UV photons from the F9 star to the inner CSE during the periastron passage. This process works because it is the products of photodissociation and photoionization that go on to form the observed SiN, SiC and NS. However, this is not the case for SiO, SiS, CS and HCN, which are considered to be parent species in most chemical models<sup>4,52</sup>. Accordingly, the effect of a stellar companion is generally not to increase the abundances of these molecules in the inner CSE, but may potentially deplete them<sup>4</sup>. Taking the case of a main-sequence companion in the inner wind, the predictions are as follows: (1) for SiO in an oxygen-rich CSE, a minimal decrease of the inner abundance is predicted, compared with a decrease of almost an order of magnitude for the carbon-rich CSE; (2) for SiS, the models predict a significant decrease of several orders of magnitude (4–6 dex) for both chemical types; however, this dramatic change could be the result of an uncertain photodissociation rate for this molecule; (3) for CS and HCN, the change in abundance for both chemical types in the presence of a stellar companion is negligible. Hence we can conclude that the asymmetric distributions seen for SiO, SiS, CS and HCN (Fig. 3 and Extended Data Fig. 4) are caused by photodissociation from the F9 companion, rather than enhanced formation during periastron.

### Hydrodynamic simulations

To better understand the structure in the CO emission, we performed high-resolution three-dimensional SPH<sup>87,88</sup> simulations of highly

eccentric systems with parameters similar to the W Aql system. These simulations were performed with the SPH code Phantom<sup>89–92</sup>. The AGB star and companion are represented by gravity-only sink particles, and the wind consists of  $\sim 7 \times 10^6$  SPH gas particles that are gradually launched from boundary shells around the AGB star, with a velocity of 13 km s<sup>-1</sup>, mimicking a free wind and a constant mass-loss rate<sup>90</sup>. Cooling within the wind is regulated by the equation of state for an ideal gas with polytropic index  $\gamma = 1.2$ , and the pulsations and rotation of the AGB star are not taken into account. It is important to note that these hydrodynamic simulations are necessarily simplified compared with observations, as they mainly account for the gravitational impact of the companion on the wind and the impact of the induced orbital movement of the AGB star, and neglect the impact of additional effects such as radiation, radiation pressure, pulsations, realistic cooling, and variable or anisotropic mass loss. We also note that the free-wind approach does not reproduce velocities lower than 13 km s<sup>-1</sup>, even though lower velocities are expected in the inner wind region (within ~80 au of the AGB star). All of these contribute to the differences between the model and observations. Hence we aim for a qualitative understanding rather than a direct fit to the data.

We present results for a model with orbital parameters close to the W Aql system, with eccentricity  $e = 0.92$  and semimajor axis  $a = 125$  au, and taking the masses of the W Aql system (see ‘Distance’). The Phantom model was evolved for around 5,000 years and the snapshot that we plot in various figures was selected from a time step a little earlier than this to better match the current positions of the two stars. From a detailed analysis of the Phantom model, we found that the orbital period increased slightly with time, owing to the mass being lost by the AGB star. This corresponded to a small increase in the semimajor axis but no change in the eccentricity over the time of the simulation. In Fig. 5c, we show the density distribution in a slice perpendicular to the orbital plane of this model. Plots of the same model showing the inner regions and a slice through the orbital plane are given in Supplementary Fig. 9. In general, we expect the companion to generate a spiral-like structure in the wind<sup>91–94</sup>. However, owing to the high eccentricity of this system, concentric near-spherical density structures are created in the wind, visible as the near-circular structures in the edge-on density distribution in Fig. 5c and Supplementary Fig. 9b. The circular structures are not quite centred on either of the central stars but rather offset to the opposite side from the F9 position at apastron, similar to the offsets we find in the ALMA CO observations. These structures are remarkably similar to the circular structures traced out by the black and white circles in Fig. 5a. The offset centres of the circles, particularly the outer circle, agree well with the observed ALMA data (white circle in Fig. 5a). Similar structures at a 90° edge-on inclination were seen for other highly eccentric SPH simulations we performed, and are also seen in previous studies with  $e = 0.8$  and a primary to secondary mass ratio of  $M_1/M_2 = 2.75$ , compared with 1.5 for the W Aql system<sup>95</sup>.

From a close study of our hydrodynamic simulations, we determine that the concentric circles are formed during the relatively quick periastron passage of the F9 star. During the periastron passage, the stars reach their maximal orbital velocity (~17 km s<sup>-1</sup> for our chosen orbital parameters) and move hyperpersonally through the wind (which has a sound speed of ~3 km s<sup>-1</sup> at 10 au), resulting in near-spherical shocks. The funnel-like structure (Fig. 5c) is formed through gravitational interactions between the companion and the wind. More concretely, when the companion moves towards the AGB star shortly before the periastron passage, its gravitational force results in a high-density wake behind the companion (see first and second columns in Supplementary Fig. 10). Because there is a velocity dispersion within this wake, it is delimited by a radially faster outer edge and a denser inner edge. As the companion and the AGB star pass each other quickly during periastron passage, the inner edge is shaped as a circular high-density shock, that travels radially outwards and expands as the left side ( $x < 0$ ) of the

three-dimensional sphere-like structure. Because the wind–companion interaction around periastron passage is strong, the outer edge of the wake becomes a bow shock after periastron passage (second and third columns of Supplementary Fig. 10)<sup>92</sup>. The formation of the spherical high-density shock is enhanced, and is completed on the right side ( $x > 0$ ), by the fast wobble of the AGB star. The orbital velocity of the stars reaches a maximum absolute value during this close encounter; however, the direction of the orbital velocity vectors changes by almost 180° due to the elliptical nature of the orbit. The wobble of the AGB creates a strong gradient in the radial wind velocity (mainly of the material on the  $x > 0$  side of the AGB, where the wind is not disturbed by the companion shock wake). The transition from faster outflowing material to slower wind particles results in a low-density region (around  $x = 40$ – $80$  au in the right column of Supplementary Fig. 10). The edge between this low-density region and the inner denser material completes the spherical high-density shock (bottom row of Supplementary Fig. 10, showing the orbit with an inclination of 90°). The spherical structures are slightly offset because of the movement of the stars. From this, and the similar results of refs. 59,95, we can conclude that such circular structures are typical of highly elliptical systems, including when those systems are seen edge-on.

We emphasize that the circular structures are a consequence of binary interaction and do not, in our model, represent a period of enhanced mass loss. This is in contrast to the simplified model of CW Leo<sup>59</sup> where the increase in density was caused by an assumed increase in mass-loss rate during periastron, in addition to the wobble of the AGB star. Some discussion of the impact of anisotropic mass loss is given in ‘Anisotropic mass loss’ in Supplementary Information. To illustrate the effect of our constant mass-loss rate, we extracted the number density of our model along the  $x$  axis with  $z = y = 0$  and compared this with the one-dimensional smooth model with an overdensity described in ‘Radiative transfer modelling’ and ref. 23. In Supplementary Fig. 11a, we show the number densities from the hydrodynamic model along the positive and negative  $x$  directions. Because the orbital parameters of our main hydrodynamic model do not precisely match the orbital parameters that we derive in this work, we performed an additional hydrodynamic model using the orbital solution discussed in ‘Orbital solutions’ ( $e = 0.93$ ,  $r_p = 10$  au). To reduce the required computational resources, we set a large accretion radius for the F9 star (1 au compared with 0.05 au in our main model), which reduces the more complex (and computationally expensive) close gravitational interactions between the companion star and the wind particles. This eliminates the funnel-like structure seen on the right of Fig. 5c but retains the sphere-like structures resulting from the motions of the two stars. For this model, the same number density plot, Supplementary Fig. 11b, reveals density peaks at radii in good agreement with the overdensity found by ref. 23. Note that, overall, the number density of the hydrodynamic models can be averaged to equal the number density of a smooth one-dimensional model (without any overdensity). However, we also note that our main model, which better allows for the close gravitational interactions between the wind and the F9 star, results in a less symmetric distribution of over- and under-dense regions (as shown for the  $x$  axis in Supplementary Fig. 11a and seen in the funnel-like structure in Fig. 5c) and contributes to the large-scale asymmetries discussed below.

On the basis of the circular structures formed during periastron, we can estimate the time of the most recent periastron from the expansion time of the black circle in Fig. 5a and the orbital period from the difference in expansion times between the black and white circles. These calculations are outlined in ‘Orbital parameters from ALMA observations’. The fact that the black circle overlaps with the edge of the SiN emission (Fig. 5b) also supports our hypothesis that the SiN was created during the most recent periastron passage.

To enable a better comparison of the SPH model with the observations, we processed the Phantom model with the radiative transfer

code MCFOST<sup>96,97</sup>, using the effective stellar temperatures of both the AGB (2,300 K) and F9 (6,000 K) stars and silicate dust from ref. 98. The computation was sped up by considering only the lowest six CO levels as this was sufficient for the task at hand. MCFOST includes a routine for determining the photodissociation of CO by the interstellar UV field<sup>99</sup>, which we used to determine the drop off in CO distribution (set to  $6 \times 10^{-4}$  relative to H<sub>2</sub> at the centre of the model), based on our three-dimensional structures. This resulted in the near-complete photodissociation of CO in the outermost density structures and left only (parts of) the innermost four circular structures visible in CO. The resultant central velocity channel is plotted in Fig. 5d, rotated to match the orientation of the W Aql system on the sky. Although the model is not a perfect reproduction of the observed CO emission (expected in light of the missing physics mentioned above), there are many qualitative similarities. We also extracted an angle–radius plot from the central channel of the MCFOST output (Supplementary Fig. 12), in which we see similar sinusoidal structures to those found in the observations (Extended Data Fig. 8 and Supplementary Fig. 4). The structures outlined by the pink and red circles identified in Fig. 5a are not apparent in the MCFOST output, although they do qualitatively resemble the structures formed at periastron. The main distinguishing feature is that the pink and red circles are offset in the opposite direction (south rather than north). If we were to ignore the offset and assume that one or both of these circles have the same origin as the black and white circles, we find that the period calculated between all the identified circles would be too short to agree with the HST and SPHERE observations of the stellar separations. Therefore, the red and pink circles cannot have formed during periastron. Noting that the Phantom model overestimates the wind velocity in the inner regions, we suggest that the difference between the observed and modelled structures partially arises from this as well as the other missing physics mentioned at the start of this section.

We also examined the channel maps generated by MCFOST at high and low velocities and compared these with equivalent channels from the ALMA observations in Extended Data Fig. 9. The observations are taken from channels  $\pm 13$  km s<sup>-1</sup> from the LSR velocity of  $v_{\text{LSR}} = -23$  km s<sup>-1</sup>. The blue channel shows CO emission elongated to the southwest, approximately along the companion axis, whereas the red channel has a more circular CO-emitting region. These differences are qualitatively reproduced in their respective MCFOST channels. This asymmetry in velocity space is also responsible for the enhanced blue emission seen in the wings of several line profiles observed towards W Aql<sup>21</sup>. The asymmetry arises from the orientation of the orbital plane such that the observations are reproduced if the Phantom model is orientated so that the motion of the F9 star at periastron is into the plane of the sky.

Finally, we comment on the large-scale asymmetry to the southwest, revealed by past observations, in the CO (ref. 22) and dust<sup>19,20</sup> emission on scales of 10'' and 60''. Although this more extended emission is in the same direction as the F9 star, the emission extent is much larger than the current or maximal separation between AGB and F9 stars ( $-0.5''$  to  $0.8''$ ; Fig. 2). The luminosity of the F9 star is insufficient for its radiation to drive the dust outwards, as the AGB star does (see ‘Radiation pressure on dust’ in Supplementary Information); instead, it contributes to the large-scale shaping of the wind through its gravitational pull. We do not detect any accretion disk around the F9 star, either in the ALMA continuum or in any molecular lines, and an accretion disk is not predicted for the W Aql system by the SPH model. However, the F9 star does gravitationally attract some circumstellar material, which is then pushed outwards by the radiation pressure from the AGB star, and results in the large-scale asymmetry seen in the dust and more extended gas<sup>19,20,22</sup>, and reproduced in our hydrodynamic model. The enhanced emission in this direction can be seen in the full extent of the central CO channel output by MCFOST (Supplementary Fig. 9c), where the CO extends out farther to the southwest.

### Orbital parameters from ALMA observations

Here we constrain some orbital parameters from the ALMA observations. First we make an estimate of the period based on the round structures seen in the CO observations. As determined in ‘Hydrodynamic simulations’, the black and white circles shown in Fig. 5 were created during periastron interactions between the AGB and F9 stars. Assuming the velocity profile from equation (2), we find the expansion time between the two circles, and hence the orbital period, through the integral:

$$T = \int_{R_{\text{black}}}^{R_{\text{white}}} \frac{dr}{v(r)} = \int_{R_{\text{black}}}^{R_{\text{white}}} \frac{dr}{v_0 + (v_\infty - v_0) \left(1 - \frac{R_{\text{in}}}{r}\right)^\beta} \quad (9)$$

where  $R_{\text{black}}$  and  $R_{\text{white}}$  are the radii of the black and white circles, and  $R_{\text{in}} = 2 \times 10^{14}$  cm is the dust condensation radius, with  $v_0 = 3$  km s<sup>-1</sup> the velocity for  $r < R_{\text{in}}$ , taken to be the sound speed<sup>21</sup>. The period is found to be  $1,082^{+89}_{-108}$  years. The uncertainty is based on the width of the circles as fit from the angle–radius plot (Extended Data Fig. 8). There we found the uncertainties in the radii of the circles to be  $10.75 \pm 0.75''$  for the white circle and  $1.35 \pm 0.10''$  for the black circle.

Another crucial parameter needed to constrain the orbital solution of the W Aql system is the time since periastron. As previously discussed, the most recent periastron passage generated the black circle seen in CO (Fig. 5) and the arc of SiN (Fig. 1). We can estimate the time of periastron by calculating the expansion time of these two structures. As we are now considering expansion in the inner part of the envelope, we need to also consider the velocity inside the dust condensation radius, which we assume to be close to the sound speed at  $v = 3$  km s<sup>-1</sup>. Equation (9) can then be rewritten:

$$\Delta t = \int_{R_{\text{in}}}^{R_{\text{black}}} \frac{dr}{v_0 + (v_\infty - v_0) \left(1 - \frac{R_{\text{in}}}{r}\right)^\beta} + \int_{R_{\text{form}}}^{R_{\text{in}}} \frac{dr}{v_0} \quad (10)$$

where  $R_{\text{black}}$  is the radius of the black circle and the radial extent of the SiN arc, and  $R_{\text{form}}$  is the radial distance at which these two structures formed.

The value of  $R_{\text{form}}$  is uncertain so we take it to be the periastron distance between stars. The smallest periastron distance we obtain is ~3 au, while the largest is equal to the dust condensation radius. Using these values as a guide and assuming a constant velocity of  $v_0 = 3$  km s<sup>-1</sup> for  $r < R_{\text{in}} = 2 \times 10^{14}$  cm, we estimate the time since the most recent periastron as  $172 \pm 22$  years ago. These derived values are listed with other orbital parameters in Supplementary Table 1.

Finally, we can determine the direction of the orbit from the position–velocity diagrams of the species formed at periastron, namely, SiN, SiC and NS. Taking into account that (1) the redder emission is brighter for all three of these molecules (and indeed only red emission is seen above the noise in the NS position–velocity diagram; Extended Data Fig. 3) and (2) the line profiles of SiN and SiC are slightly blueshifted relative to the stellar LSR velocity, suggests that these species formed first on the blue side of the envelope and then more recently on the red side. Hence, there has been slightly more time for the blue emission to expand, shifting the line profiles and position–velocity diagrams bluewards. From this, we conclude that the direction of the periastron passage was, for the F9 star, into the plane of the sky. This agrees with the evidence from the SPH model discussed above.

### Orbital solutions

The orbit of the W Aql system cannot be solved analytically, so instead we solve it numerically by calculating a series of possible orbits and checking which agree with the parameters derived from observations (that is, the parameters listed in Supplementary Table 1). We adjust our basic orbital solution by leaving as free parameters the eccentricity,  $e$ ,

and the periastron distance,  $r_p$ . All other primary orbital parameters are either input from previous results or calculated from  $e$  and  $r_p$  as follows.

The apastron,  $r_a$ , is defined by

$$r_a = r_p \left( \frac{e+1}{1-e} \right) \quad (11)$$

and the semimajor axis,  $a$ , is then

$$a = \frac{r_p + r_a}{2}. \quad (12)$$

Working in the reference frame of the AGB star, we define the focus of the ellipse traced by the F9 star as the location of the AGB star, defined here as (0, 0, 0) in our Cartesian co-ordinate scheme.

From the system mass ( $M + m = 2.66 M_\odot$ ) and the semimajor axis, we can then calculate the orbital period,  $T$

$$T = 2\pi \sqrt{\frac{a^3}{G(M+m)}}. \quad (13)$$

where  $G$  is the gravitational constant and  $M$  and  $m$  are the masses of the AGB and F9 stars. This is enough information to plot a top-down view of the orbit, as shown in Supplementary Fig. 13. However, we know from observations that the orbit is inclined and rotated in the plane of the sky (relative to north). From the observations of SiN, we estimate the inclination angle of the orbit to be close to edge-on,  $i = 90 \pm 7^\circ$ . We plot  $i = 85^\circ$  to better illustrate the orbit in the plane of the sky, but note that a completely edge-on system ( $i = 90^\circ$ ) satisfies the observations and does not significantly change our results. From the photometry of the two stars, we rotate the orbit in the plane of the sky by  $\omega = 120^\circ$  to fit the SPHERE observation (Fig. 2). We note that the uncertainty in  $\omega$  comes mainly from the precise values of the inclination and eccentricity, but the selection of  $\omega = 120^\circ$  is a good fit given the rest of our results. The sky projection of a selected orbit and the locations of the stars are plotted in Fig. 2. We assume no rotation out of the plane of the sky along the third orthogonal axis because the relative symmetry of the SiN position–velocity diagram (Fig. 1b) suggests that this value is small ( $<5^\circ$ ).

For a possible orbital solution, we must calculate the time since periastron and the time between the SPHERE and HST observations. For this we must consider the angle  $\theta$  made between the periastron, the AGB star and the F9 star, as well as the eccentric anomaly,  $E$ . Both of these angles are shown in Supplementary Fig. 13 and are mathematically related by

$$\tan\left(\frac{\theta}{2}\right) = \tan\left(\frac{E}{2}\right) \sqrt{\frac{1+e}{1-e}} \quad (14)$$

$$E = 2 \tan^{-1} \left( \tan\left(\frac{\theta}{2}\right) \sqrt{\frac{1-e}{1+e}} \right). \quad (15)$$

The time since periastron,  $\Delta t$ , can then be calculated

$$\Delta t = \frac{T}{2\pi} (E - e \sin(E)). \quad (16)$$

We also check the possible solution against the known time between the HST and SPHERE observations by comparing  $\Delta t_{\text{SPHERE}} - \Delta t_{\text{HST}}$  against the time difference between those observations.

To find the best solutions, we modify the input parameters ( $r_p$  and  $e$ ) until we find a suitable orbit that agrees with the values we found for the period, time since periastron and time between HST and SPHERE observations. Because of the uncertainties, we find a group of compatible solutions rather than one single definition of the orbit. From a grid with steps of  $\Delta e = 0.01 \in [0.70, 0.99]$  and

$\Delta r_p = 0.1 \times 10^{14}$  cm  $\in [0.4 \times 10^{14}$  cm,  $5 \times 10^{14}$  cm], we found a set of compatible solutions, all of which are given in Extended Data Table 1. For the highest eccentricities  $e > 0.95$  we additionally tested a finer grid for  $r_p$ , with  $\Delta r_p = 0.5 \times 10^{13}$  cm  $\in [5 \times 10^{13}$  cm,  $1 \times 10^{14}$  cm], because the orbital timing becomes sensitive to small variations in  $r_p$  at these high eccentricities. The compatible solutions range from the extremes of  $e = 0.98$ ,  $r_p = 4.5 \times 10^{13}$  cm to  $e = 0.91$ ,  $r_p = 2.0 \times 10^{14}$  cm. We plot one of these solutions ( $e = 0.93$ ,  $r_p = 1.5 \times 10^{14}$  cm) in Fig. 2, where we also show the orbit superposed on the HST and SPHERE photometric observations. Note that although some of our solutions have very small periastron distances, none are smaller than the Roche limit, so direct accretion of the AGB star onto the F9 star is not expected.

In Extended Data Table 1, we also include  $t_{\text{close}}$ , which we define as the time the AGB and F9 stars spend ‘close’ to each other. More precisely, in the AGB frame, this is the time the F9 star takes to pass through the  $-90^\circ \leq \theta \leq 90^\circ$  region of the orbit (Supplementary Fig. 13) and can be derived from equations (15) and (16). As noted in Extended Data Table 1,  $t_{\text{close}}$  ranges from 2 years at the highest eccentricity to 18 years at  $e = 0.91$ . This corresponds to  $-0.1\%$  to  $2\%$  of the total orbital period.

## Data availability

The observational data used here are openly available through the data archives for ALMA (<https://almascience.nrao.edu/aq/>), ESO for the APEX and SPHERE data (<http://archive.eso.org>), and HST (<https://hla.stsci.edu>). Custom ALMA data products that were produced for this study are available from T.D. or A.M.S.R. (a.m.s.richards@manchester.ac.uk) upon reasonable request. The Phantom input and output files from our main model can be downloaded from <https://doi.org/10.26180/24240001.v1>.

## Code availability

Phantom is open source under the GPLv3 license and can be downloaded via <https://github.com/danieljprice/phantom>. MCFOST is open source under the GPLv3 license and can be downloaded via <https://mcfost.readthedocs.io/en/latest/overview.html>. ALI, the one-dimensional radiative transfer code, is available from the corresponding author upon reasonable request.

## References

- Höfner, S. & Olofsson, H. Mass loss of stars on the asymptotic giant branch. Mechanisms, models and measurements. *Astron. Astrophys. Rev.* **26**, 1 (2018).
- Kobayashi, C., Karakas, A. I. & Lugaro, M. The origin of elements from carbon to uranium. *Astrophys. J.* **900**, 179 (2020).
- Decin, L. et al. Reduction of the maximum mass-loss rate of OH/IR stars due to unnoticed binary interaction. *Nat. Astron.* **3**, 408–415 (2019).
- Van de Sande, M. & Millar, T. J. The impact of stellar companion UV photons on the chemistry of the circumstellar environments of AGB stars. *Mon. Not. R. Astron. Soc.* **510**, 1204–1222 (2022).
- De Marco, O. et al. The messy death of a multiple star system and the resulting planetary nebula as observed by JWST. *Nat. Astron.* **6**, 1421–1432 (2022).
- Decin, L. et al. (Sub)stellar companions shape the winds of evolved stars. *Science* **369**, 1497–1500 (2020).
- Jorissen, A. in *Asymptotic Giant Branch Stars* (eds. H. J. Habing & H. Olofsson) 461–518 (Springer, 2004).
- Karovska, M., Hack, W., Raymond, J. & Guinan, E. First Hubble Space Telescope observations of Mira AB wind-accreting binary systems. *Astrophys. J. Lett.* **482**, 175–178 (1997).
- Ramstedt, S. et al. The wonderful complexity of the Mira AB system. *Astron. Astrophys.* **570**, 14 (2014).
- Kervella, P. et al. ALMA observations of the nearby AGB star L<sub>2</sub> Puppis. I. Mass of the central star and detection of a candidate planet. *Astron. Astrophys.* **596**, 92 (2016).
- Homan, W. et al. ATOMIUM: a high-resolution view on the highly asymmetric wind of the AGB star  $\pi^1$  Gruis. I. First detection of a new companion and its effect on the inner wind. *Astron. Astrophys.* **644**, 61 (2020).
- Mauron, N. & Huggins, P. J. Imaging the circumstellar envelopes of AGB stars. *Astron. Astrophys.* **452**, 257–268 (2006).
- Kim, H. et al. The large-scale nebular pattern of a superwind binary in an eccentric orbit. *Nat. Astron.* **1**, 0060 (2017).
- Maercker, M. et al. Unexpectedly large mass loss during the thermal pulse cycle of the red giant star R Sculptoris. *Nature* **490**, 232–234 (2012).
- Sahai, R. et al. The rapidly evolving asymptotic giant branch star, V Hya: ALMA finds a multiring circus with high-velocity outflows. *Astrophys. J.* **929**, 59 (2022).
- Ramos-Larios, G. et al. Rings and arcs around evolved stars—I. Fingerprints of the last gasps in the formation process of planetary nebulae. *Mon. Not. R. Astron. Soc.* **462**, 610–635 (2016).
- Herbig, G. H. Physical companions to long-period variables. *Veroeffentlichungen der Remeis-Sternwarte zu Bamberg* **27**, 164 (1965).
- Danilovich, T., Olofsson, G., Black, J. H., Justtanont, K. & Olofsson, H. Classifying the secondary component of the binary star W Aquilae. *Astron. Astrophys.* **574**, 23 (2015).
- Ramstedt, S., Maercker, M., Olofsson, G., Olofsson, H. & Schöier, F. L. Imaging the circumstellar dust around AGB stars with PolCor. *Astron. Astrophys.* **531**, 148 (2011).
- Mayer, A. et al. Large-scale environments of binary AGB stars probed by Herschel. I. Morphology statistics and case studies of R Aquarii and W Aquilae. *Astron. Astrophys.* **549**, 69 (2013).
- Danilovich, T. et al. Detailed modelling of the circumstellar molecular line emission of the S-type AGB star W Aquilae. *Astron. Astrophys.* **569**, 76 (2014).
- Ramstedt, S. et al. The circumstellar envelope around the S-type AGB star W Aql. Effects of an eccentric binary orbit. *Astron. Astrophys.* **605**, 126 (2017).
- Brunner, M. et al. Molecular line study of the S-type AGB star W Aquilae. ALMA observations of CS, SiS, SiO and HCN. *Astron. Astrophys.* **617**, 23 (2018).
- Danilovich, T. et al. ATOMIUM: halide molecules around the S-type AGB star W Aquilae. *Astron. Astrophys.* **655**, 80 (2021).
- Richichi, A., Percheron, I. & Khristoforova, M. CHARM2: an updated catalog of high angular resolution measurements. *Astron. Astrophys.* **431**, 773–777 (2005).
- Turner, B. E. Detection of SiN in IRC+10216. *Astrophys. J. Lett.* **388**, 35 (1992).
- Huggins, P. J., Glassgold, A. E. & Morris, M. CN and C<sub>2</sub>H in IRC+10216. *Astrophys. J.* **279**, 284–290 (1984).
- Tokovinin, A. & Kiyaveva, O. Eccentricity distribution of wide binaries. *Mon. Not. R. Astron. Soc.* **456**, 2070–2079 (2016).
- Boffin, H. M. J., Cerf, N. & Paulus, G. Statistical analysis of a sample of spectroscopic binaries containing late-type giants. *Astron. Astrophys.* **271**, 125–138 (1993).
- Moe, M. & Di Stefano, R. Mind your Ps and Qs: the interrelation between period (P) and mass-ratio (Q) distributions of binary stars. *Astrophys. J. Suppl. Ser.* **230**, 15 (2017).
- Maercker, M. et al. A detailed view of the gas shell around R Sculptoris with ALMA. *Astron. Astrophys.* **586**, 5 (2016).
- Lykou, F. et al. The curious case of II Lup: a complex morphology revealed with SAM/NACO and ALMA. *Mon. Not. R. Astron. Soc.* **480**, 1006–1021 (2018).
- Doan, L. et al. The extended molecular envelope of the asymptotic giant branch star  $\pi^1$  Gruis as seen by ALMA. I. Large-scale kinematic structure and CO excitation properties. *Astron. Astrophys.* **605**, 28 (2017).

34. Sahai, R., Scibelli, S. & Morris, M. R. High-speed bullet ejections during the AGB-to-planetary nebula transition: HST observations of the carbon star, V Hydrae. *Astrophys. J.* **827**, 92 (2016).
35. Oomen, G.-M. et al. Orbital properties of binary post-AGB stars. *Astron. Astrophys.* **620**, 85 (2018).
36. Jorissen, A., Van Eck, S., Mayor, M. & Udry, S. Insights into the formation of barium and Tc-poor S stars from an extended sample of orbital elements. *Astron. Astrophys.* **332**, 877–903 (1998).
37. Ramstedt, S., Schöier, F. L. & Olofsson, H. Circumstellar molecular line emission from S-type AGB stars: mass-loss rates and SiO abundances. *Astron. Astrophys.* **499**, 515–527 (2009).
38. Knapp, G. R. & Morris, M. Mass loss from evolved stars. III—Mass loss rates for fifty stars from CO  $J=1-0$  observations. *Astrophys. J.* **292**, 640–669 (1985).
39. Jura, M. Mass loss from S stars. *Astrophys. J. Suppl. Ser.* **66**, 33 (1988).
40. Groenewegen, M. A. T. & De Jong, T. CO observations and mass loss of MS- and S-stars. *Astron. Astrophys.* **337**, 797–807 (1998).
41. Gaia Collaboration The Gaia mission. *Astron. Astrophys.* **595**, 1 (2016).
42. Andriantsaralaza, M., Ramstedt, S., Vlemmings, W. H. T. & De Beck, E. Distance estimates for AGB stars from parallax measurements. *Astron. Astrophys.* **667**, 74 (2022).
43. Gaia Collaboration Gaia Early Data Release 3. Summary of the contents and survey properties. *Astron. Astrophys.* **649**, 1 (2021).
44. Habets, G. M. H. J. & Heintze, J. R. W. Empirical bolometric corrections for the main-sequence. *Astron. Astrophys. Suppl. Ser.* **46**, 193–237 (1981).
45. De Nutte, R. et al. Nucleosynthesis in AGB stars traced by oxygen isotopic ratios. I. Determining the stellar initial mass by means of the  $^{17}\text{O}/^{16}\text{O}$  ratio. *Astron. Astrophys.* **600**, 71 (2017).
46. De Beck, E. & Olofsson, H. The surprisingly carbon-rich environment of the S-type star W Aql. *Astron. Astrophys.* **642**, 20 (2020).
47. Vassiliadis, E. & Wood, P. R. Evolution of low- and intermediate-mass stars to the end of the asymptotic giant branch with mass loss. *Astrophys. J.* **413**, 641–657 (1993).
48. Montargès, M. et al. The VLT/SPHERE view of the ATOMIUM cool evolved star sample. I. Overview: sample characterization through polarization analysis. *Astron. Astrophys.* **671**, 96 (2023).
49. Maire, A.-L. et al. High-precision astrometric studies in direct imaging with SPHERE. *The Messenger* **183**, 7–12 (2021).
50. Gottlieb, C. A. et al. ATOMIUM: ALMA tracing the origins of molecules in dust forming oxygen rich M-type stars. Motivation, sample, calibration, and initial results. *Astron. Astrophys.* **660**, 94 (2022).
51. The CASA Team et al. CASA, the Common Astronomy Software Applications for radio astronomy. *Publ. Astron. Soc. Pacific* **134**, 114501 (2022).
52. Thompson, A. R., Moran, J. M. & Swenson, G. W. Jr *Interferometry and Synthesis in Radio Astronomy* 3rd edn (Springer, 2017).
53. Olofsson, H., Eriksson, K., Gustafsson, B. & Carlstrom, U. A study of circumstellar envelopes around bright carbon stars. I—Structure, kinematics, and mass-loss rate. *Astrophys. J. Suppl. Ser.* **87**, 267–304 (1993).
54. Homan, W. et al. ATOMIUM: the astounding complexity of the near circumstellar environment of the M-type AGB star R Hydrae. I. Morpho-kinematical interpretation of CO and SiO emission. *Astron. Astrophys.* **651**, 82 (2021).
55. Vlemmings, W. H. T., Khouri, T. & Olofsson, H. Resolving the extended stellar atmospheres of asymptotic giant branch stars at (sub)millimetre wavelengths. *Astron. Astrophys.* **626**, 81 (2019).
56. Baudry, A. et al. ATOMIUM: probing the inner wind of evolved O-rich stars with new, highly excited H<sub>2</sub>O and OH lines. *Astron. Astrophys.* **674**, 125 (2023).
57. Cernicharo, J., Gottlieb, C. A., Guelin, M., Thaddeus, P. & Vrtilek, J. M. Astronomical and laboratory detection of the SiC radical. *Astrophys. J. Lett.* **341**, 25 (1989).
58. Massalkhi, S. et al. Abundance of SiC<sub>2</sub> in carbon star envelopes. *Astron. Astrophys.* **611**, 29 (2018).
59. Cernicharo, J., Marcelino, N., Agúndez, M. & Guélin, M. Molecular shells in IRC+10216: tracing the mass loss history. *Astron. Astrophys.* **575**, 91 (2015).
60. Decin, L. et al. ALMA data suggest the presence of spiral structure in the inner wind of CW Leonis. *Astron. Astrophys.* **574**, 5 (2015).
61. Siebert, M. A., Van de Sande, M., Millar, T. J. & Remijan, A. J. Investigating anomalous photochemistry in the inner wind of IRC+10216 through interferometric observations of HC<sub>3</sub>N. *Astrophys. J.* **941**, 90 (2022).
62. Patel, N., Gottlieb, C. & Young, K. Probing the dust formation zone in IRC+10216 with the SMA. In *Proc. The Life Cycle of Dust in the Universe: Observations* (eds Kemper et al.) 98 (2013).
63. Velilla-Prieto, L. et al. Circumstellar chemistry of Si-C bearing molecules in the C-rich AGB star IRC+10216. *IAU Symp.* **343**, 535–537 (2019).
64. Lee, S. K., Ozeki, H. & Saito, S. Microwave spectrum of the NS radical in the  $^2\Pi$  ground electronic state. *Astrophys. J. Suppl. Ser.* **98**, 351 (1995).
65. Velilla Prieto, L. et al. The millimeter IRAM-30 m line survey toward IK Tauri. *Astron. Astrophys.* **597**, 25 (2017).
66. Decin, L., Richards, A. M. S., Danilovich, T., Homan, W. & Nuth, J. A. ALMA spectral line and imaging survey of a low and a high mass-loss rate AGB star between 335 and 362 GHz. *Astron. Astrophys.* **615**, 28 (2018).
67. Decin, L. et al. Discovery of multiple dust shells beyond 1 arcmin in the circumstellar envelope of IRC+10216 using Herschel/PACS. *Astron. Astrophys.* **534**, 1 (2011).
68. Guélin, M. et al. IRC +10 216 in 3D: morphology of a TP-AGB star envelope. *Astron. Astrophys.* **610**, 4 (2018).
69. Schöier, F. L. et al. The abundance of HCN in circumstellar envelopes of AGB stars of different chemical type. *Astron. Astrophys.* **550**, 78 (2013).
70. Danilovich, T. et al. Sulphur-bearing molecules in AGB stars. II. Abundances and distributions of CS and SiS. *Astron. Astrophys.* **617**, 132 (2018).
71. Massalkhi, S., Agúndez, M. & Cernicharo, J. Study of CS, SiO, and SiS abundances in carbon star envelopes: assessing their role as gas-phase precursors of dust. *Astron. Astrophys.* **628**, 62 (2019).
72. Morris, M. & Jura, M. Molecular self-shielding in the outflows from late-type stars. *Astrophys. J.* **264**, 546–553 (1983).
73. Bachiller, R. et al. A survey of CN in circumstellar envelopes. *Astron. Astrophys.* **319**, 235–243 (1997).
74. Rybicki, G. B. & Hummer, D. G. An accelerated lambda iteration method for multilevel radiative transfer. I—Non-overlapping lines with background continuum. *Astron. Astrophys.* **245**, 171–181 (1991).
75. Pickett, H. M. The fitting and prediction of vibration–rotation spectra with spin interactions. *J. Mol. Spectrosc.* **148**, 371–377 (1991).
76. Lique, F. et al. Rotational excitation of CN( $X^2\Sigma^+$ ) by He: theory and comparison with experiments. *J. Chem. Phys.* **132**, 024303 (2010).
77. Montez Jr, R., Ramstedt, S., Kastner, J. H., Vlemmings, W. & Sanchez, E. A catalog of GALEX ultraviolet emission from asymptotic giant branch stars. *Astrophys. J.* **841**, 33 (2017).
78. Schrijver, C. J. Magnetic structure in cool stars. XI. Relations between radiative fluxes measuring stellar activity, and evidence for two components in stellar chromospheres. *Astron. Astrophys.* **172**, 111–123 (1987).

79. Gálvez, M. C. et al. Multiwavelength optical observations of chromospherically active binary systems. IV. The X-ray/EUV selected binary BK Psc (2RE J0039+103). *Astron. Astrophys.* **389**, 524–536 (2002).
80. Gray, R. O., Corbally, C. J. & Burgasser, A. J. *Stellar Spectral Classification* Princeton Series in Astrophysics (Princeton Univ. Press, 2009); [http://books.google.com.au/books?id=S\\_Sh1i226wwC](http://books.google.com.au/books?id=S_Sh1i226wwC)
81. Asplund, M., Amarsi, A. M. & Grevesse, N. The chemical make-up of the Sun: a 2020 vision. *Astron. Astrophys.* **653**, 141 (2021).
82. Agúndez, M., Martínez, J. I., de Andres, P. L., Cernicharo, J. & Martín-Gago, J. A. Chemical equilibrium in AGB atmospheres: successes, failures, and prospects for small molecules, clusters, and condensates. *Astron. Astrophys.* **637**, 59 (2020).
83. Agúndez, M. et al. Growth of carbon chains in IRC+10216 mapped with ALMA. *Astron. Astrophys.* **601**, 4 (2017).
84. Cordiner, M. A. & Millar, T. J. Density-enhanced gas and dust shells in a new chemical model for IRC+10216. *Astrophys. J.* **697**, 68–78 (2009).
85. Kerkines, I. S. K. & Mavridis, A. On the electron affinity of SiN and spectroscopic constants of SiN<sup>-</sup>. *J. Chem. Phys.* **123**, 124301–124301 (2005).
86. Thomson, R. & Dalby, F. W. Experimental determination of the dipole moments of the X(<sup>2</sup>Σ<sup>+</sup>) and B(<sup>2</sup>Σ<sup>+</sup>) states of the CN molecule. *Can. J. Phys.* **46**, 2815 (1968).
87. Monaghan, J. J. Smoothed particle hydrodynamics. *Rep. Prog. Phys.* **68**, 1703–1759 (2005).
88. Price, D. J. Smoothed particle hydrodynamics and magnetohydrodynamics. *J. Comput. Phys.* **231**, 759–794 (2012).
89. Price, D. J. et al. Phantom: a smoothed particle hydrodynamics and magnetohydrodynamics code for astrophysics. *Publ. Astron. Soc. Aust.* **35**, 031 (2018).
90. Siess, L., Homan, W., Toupin, S. & Price, D. J. 3D simulations of AGB stellar winds. I. Steady winds and dust formation. *Astron. Astrophys.* **667**, 75 (2022).
91. Maes, S. et al. SPH modelling of companion-perturbed AGB outflows including a new morphology classification scheme. *Astron. Astrophys.* **653**, 25 (2021).
92. Malfait, J. et al. SPH modelling of wind-companion interactions in eccentric AGB binary systems. *Astron. Astrophys.* **652**, 51 (2021).
93. Mastrodemos, N. & Morris, M. Bipolar preplanetary nebulae: hydrodynamics of dusty winds in binary systems. I. Formation of accretion disks. *Astrophys. J.* **497**, 303–329 (1998).
94. Mastrodemos, N. & Morris, M. Bipolar pre-planetary nebulae: hydrodynamics of dusty winds in binary systems. II. Morphology of the circumstellar envelopes. *Astrophys. J.* **523**, 357–380 (1999).
95. Kim, H., Liu, S.-Y. & Taam, R. E. Templates of binary-induced spiral-shell patterns around mass-losing post-main-sequence stars. *Astrophys. J. Suppl. Ser.* **243**, 35 (2019).
96. Pinte, C., Ménard, F., Duchêne, G. & Bastien, P. Monte Carlo radiative transfer in protoplanetary disks. *Astron. Astrophys.* **459**, 797–804 (2006).
97. Pinte, C. et al. Benchmark problems for continuum radiative transfer. High optical depths, anisotropic scattering, and polarisation. *Astron. Astrophys.* **498**, 967–980 (2009).
98. Weingartner, J. C. & Draine, B. T. Dust grain-size distributions and extinction in the Milky Way, Large Magellanic Cloud, and Small Magellanic Cloud. *Astrophys. J.* **548**, 296–309 (2001).
99. Pinte, C. et al. Direct mapping of the temperature and velocity gradients in discs. Imaging the vertical CO snow line around IM Lupi. *Astron. Astrophys.* **609**, 47 (2018).
100. Winnewisser, G., Belov, S. P., Klaus, T. & Schieder, R. Sub-Doppler measurements on the rotational transitions of carbon monoxide. *J. Mol. Spectrosc.* **184**, 468–472 (1997).
101. Bogey, M., Demuyneck, C. & Destombes, J. L. Laboratory measurement of the submillimeter wave spectrum of SiC and isotopomers. *Astron. Astrophys.* **232**, 19 (1990).
102. Yamada, K. M. T., Moravec, A. & Winnewisser, G. Sub-millimeter wave spectra of cyanoacetylene and revised ground state constants. *Z. Naturforsch.* **A 50**, 1179–1181 (1995).
103. Müller, H. S. P. et al. Rotational spectroscopy of isotopologues of silicon monoxide, SiO, and spectroscopic parameters from a combined fit of rotational and rovibrational data. *J. Phys. Chem. A* **117**, 13843–13854 (2013).
104. Müller, H. S. P. et al. Rotational spectroscopy of the isotopic species of silicon monosulfide, SiS. *Phys. Chem. Chem. Phys.* **9**, 1579 (2007).
105. Gottlieb, C. A., Myers, P. C. & Thaddeus, P. Precise millimeter-wave laboratory frequencies for CS and C<sup>34</sup>S. *Astrophys. J.* **588**, 655–661 (2003).
106. Ahrens, V. et al. Sub-Doppler saturation spectroscopy of HCN up to 1 THz and detection of  $J = 3 \rightarrow 2$  ( $4 \rightarrow 3$ ) emission from TMC1. *Z. Naturforsch.* **A 57**, 669–681 (2002).
107. Fuchs, U. et al. High resolution spectroscopy of HCN isotopomers: H<sup>13</sup>CN, HC<sup>15</sup>N, and H<sup>13</sup>C<sup>15</sup>N in the ground and first excited bending vibrational state. *Z. Naturforsch.* **A 59**, 861–872 (2004).
108. Bogey, M., Demuyneck, C. & Destombes, J. L. The millimetre wave spectrum of the <sup>13</sup>C<sup>14</sup>N radical in its ground state. *Can. J. Phys.* **62**, 1248–1253 (1984).
109. Müller, H. S. P., Thorwirth, S., Roth, D. A. & Winnewisser, G. The Cologne Database for Molecular Spectroscopy, CDMS. *Astron. Astrophys.* **370**, 49–52 (2001).
110. Müller, H. S. P., Schlöder, F., Stutzki, J. & Winnewisser, G. The Cologne Database for Molecular Spectroscopy, CDMS: a useful tool for astronomers and spectroscopists. *J. Mol. Struct.* **742**, 215–227 (2005).

## Acknowledgements

We thank S.-H. Cho of the Korean VLBI Network for KVN observations of W Aql to confirm consistency with our ALMA results. T.D. is supported in part by the Australian Research Council through a Discovery Early Career Researcher Award (DE230100183). T.D., F.D.C. and S.H.J.W. acknowledge support from the Research Foundation Flanders (FWO) through grants 12N9920N, 1253223N and 1285221N, respectively. J.M. and S.M. acknowledge support from the Research Foundation Flanders (FWO) grant G099720N. M.V.d.S. acknowledges support from European Union's Horizon 2020 Research and Innovation programme under the Marie Skłodowska-Curie grant agreement number 882991. M.M. acknowledges funding from the Programme Paris Region fellowship supported by the Région Ile-de-France. P.K. acknowledges funding from the European Research Council (ERC) under the European Union's Horizon 2020 Research and Innovation programme (synergy grant project UniverScale, grant agreement 951549). T.J.M. is grateful to the STFC for support through grant ST/P000312/1 and thanks the Leverhulme Trust for the award of an Emeritus Fellowship. J.M.C.P. was supported by STFC grant number ST/T000287/1. L.D., J.M.C.P., S.H.J.W., S.M. and D.G. acknowledge support from ERC consolidator grant 646758 AEROSOL. E.D.B. acknowledges support from the Swedish National Space Agency. D.G. was funded by the project grant 'The Origin and Fate of Dust in Our Universe' from the Knut and Alice Wallenberg Foundation. K.T.W. acknowledges support from the European Research Council (ERC) under the European Union's Horizon 2020 Research and Innovation programme (grant agreement number 883867, project EXWINGS). F.H., A.B. and L.M. acknowledge funding from the French National Research Agency (ANR) project PEPPER (ANR-20-CE31-0002). H.S.P.M. acknowledges support by the Deutsche Forschungsgemeinschaft through the collaborative research grant SFB 956 (project ID 184018867). R.S.'s contribution to the research described here was

carried out at the Jet Propulsion Laboratory, California Institute of Technology, under a contract with NASA, and funded in part by NASA via ADAP awards, and multiple HST GO awards from the Space Telescope Science Institute. A.Z. is funded by STFC/UKRI through grant ST/T000414/1. This research was supported in part by the Australian Research Council Centre of Excellence for All Sky Astrophysics in 3 Dimensions (ASTRO 3D), through project number CE170100013. This project has received funding from the Framework Program for Research and Innovation 'Horizon 2020' under the convention Marie Skłodowska-Curie No 945298. Computational resources and services used in this work were provided by the VSC (Flemish Supercomputer Center), funded by the Research Foundation Flanders (FWO) and the Flemish Government, department EWI. This research was undertaken with the assistance of resources and services from the National Computational Infrastructure (NCI), which is supported by the Australian Government. This paper makes use of the following ALMA data: ADS/JAO.ALMA#2018.1.00659.L. ALMA is a partnership of ESO (representing its member states), NSF (USA) and NINS (Japan), together with NRC (Canada), MOST and ASIAA (Taiwan), and KASI (Republic of Korea), in cooperation with the Republic of Chile. The Joint ALMA Observatory is operated by ESO, AUI/NRAO and NAOJ. Based on observations collected at the European Organisation for Astronomical Research in the Southern Hemisphere under ESO programme 0103.D-0772(A). We acknowledge excellent support from the UK ALMA Regional Centre (UK ARC), which is hosted by the Jodrell Bank Centre for Astrophysics (JBCA) at the University of Manchester. The UK ARC Node is supported by STFC Grant ST/P000827/1.

### Author contributions

T.D. conceived of and led this publication, analysed and interpreted data, performed the radiative transfer models, wrote the paper, and created most of the figures. J.M. performed and interpreted the hydrodynamics model and made Fig. 5c, and Supplementary Figs. 9a,b and 10. M.V.d.S. led the chemical interpretation and made Supplementary Figs. 7 and 8. M.M. and P.K. contributed the analysis of the resolved imaging. A.M.S.R. performed the ALMA data reduction. F.D.C. and A.C. contributed to the three-dimensional interpretation of the data. T.J.M. and J.M.C.P. contributed to the chemical interpretation. C.A.G. contributed to the line identifications and interpretation.

C.P. assisted in the MCFOST modelling. D.J.P. assisted in the Phantom modelling and interpretation. E.D.B. contributed the fully reduced APEX data. The ALMA proposal was led by L.D. and C.A.G., with contributions from M.M., T.D., A.d.K., K.M.M., R.S., A.M.S.R., J.M.C.P., H.S.P.M., E.D.B., P.K., A.B., K.T.W., M.V.d.S., E.L., D.G., J.Y. and D.J.P. All authors contributed to discussions of the results, and commented on the paper and analysis.

### Competing interests

The authors declare no competing interests.

### Additional information

**Extended data** is available for this paper at <https://doi.org/10.1038/s41550-023-02154-y>.

**Supplementary information** The online version contains supplementary material available at <https://doi.org/10.1038/s41550-023-02154-y>.

**Correspondence and requests for materials** should be addressed to T. Danilovich.

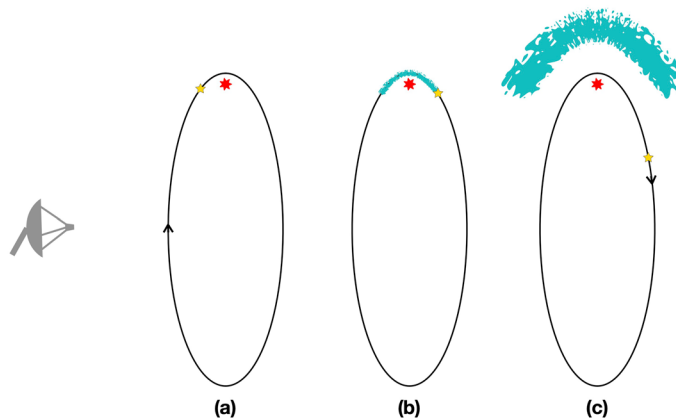
**Peer review information** *Nature Astronomy* thanks the anonymous reviewers for their contribution to the peer review of this work.

**Reprints and permissions information** is available at [www.nature.com/reprints](http://www.nature.com/reprints).

**Publisher's note** Springer Nature remains neutral with regard to jurisdictional claims in published maps and institutional affiliations.

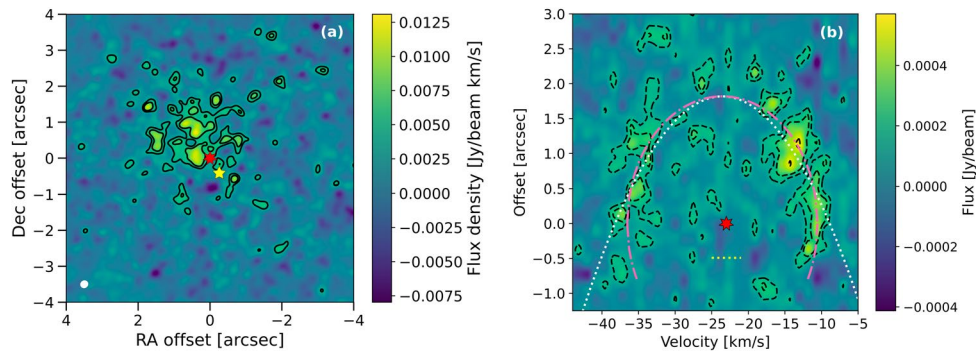
Springer Nature or its licensor (e.g. a society or other partner) holds exclusive rights to this article under a publishing agreement with the author(s) or other rightsholder(s); author self-archiving of the accepted manuscript version of this article is solely governed by the terms of such publishing agreement and applicable law.

© The Author(s), under exclusive licence to Springer Nature Limited 2023



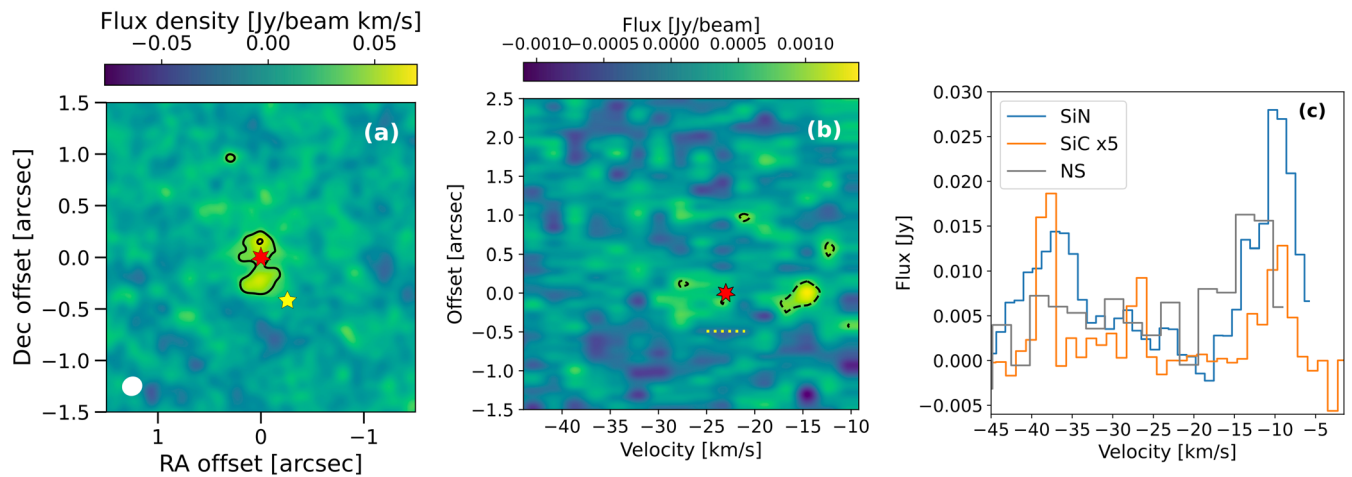
**Extended Data Fig. 1 | A series of sketches illustrating the formation of SiN during the periastron passage of the W Aql system.** The orbit (black line) is shown face on in the frame of the AGB star and the F9 star is assumed to be moving clockwise. Relative to our observations, the observer is located to the left, represented by the radio dish. **(a)** The F9 star (yellow) approaches the AGB star (red) and enters the dense inner wind region ( $n_{\text{H}_2} \sim 10^8$  to  $10^{10} \text{ cm}^{-3}$ ). **(b)** The rapid periastron passage is completed and SiN (and, similarly, SiC and NS) has

formed in the wake of the F9 star (cyan region), with formation initiated by the F9 UV flux (see ‘Chemical modelling’ in the Methods). **(c)** As the F9 star continues on its orbit, the arc of SiN expands away from the AGB star, along with the stellar wind in which it is embedded. The present-day configuration of SiN can be seen in Fig. 1, where the PV diagram is a good approximation of the final arc shape that would be seen around the AGB star were the orbit viewed face-on.



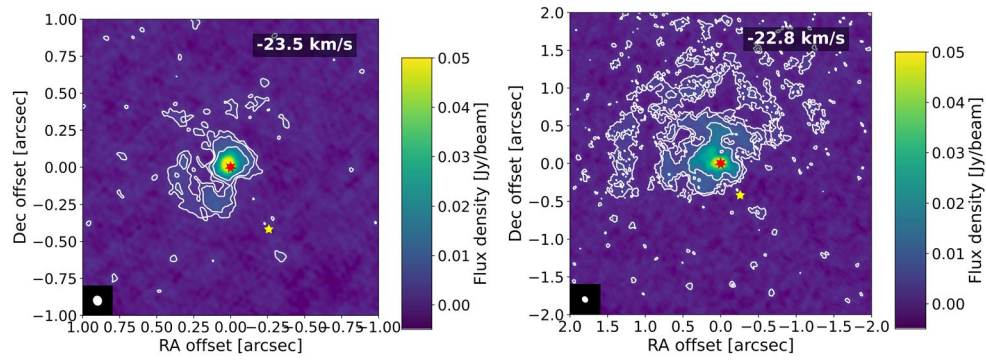
**Extended Data Fig. 2 | Observed SiC emission towards W Aql.** (a) Zeroth moment map of SiC towards W Aql with contours at levels of  $3\sigma$  and  $5\sigma$ . Transition details are given in Table 1. North is up and east is to the left. The position of the AGB star is indicated by the red star at (0,0) and the location of the F9 companion is indicated by the yellow star to the south-west. North is up and east is left. The white ellipse in the bottom left corner indicates the size of the synthesized beam. (b) Position-velocity diagram of SiC towards W Aql, taken with the same wide

slit as used for SiN (Fig. 1), with a position angle of north  $33^\circ$  east. Dashed black contours are at levels of  $3\sigma$  and  $5\sigma$ , a dotted white parabola is fit to the data (see ‘SiN and SiC’ in the ‘Data reduction’ section in the Methods), and a dash-dotted pink ellipse is plotted to emphasize the shape of the emission in the PV diagram. The position and LSR velocity of the AGB star is indicated by the red star and the horizontal yellow dotted line indicates the present offset of the F9 star.



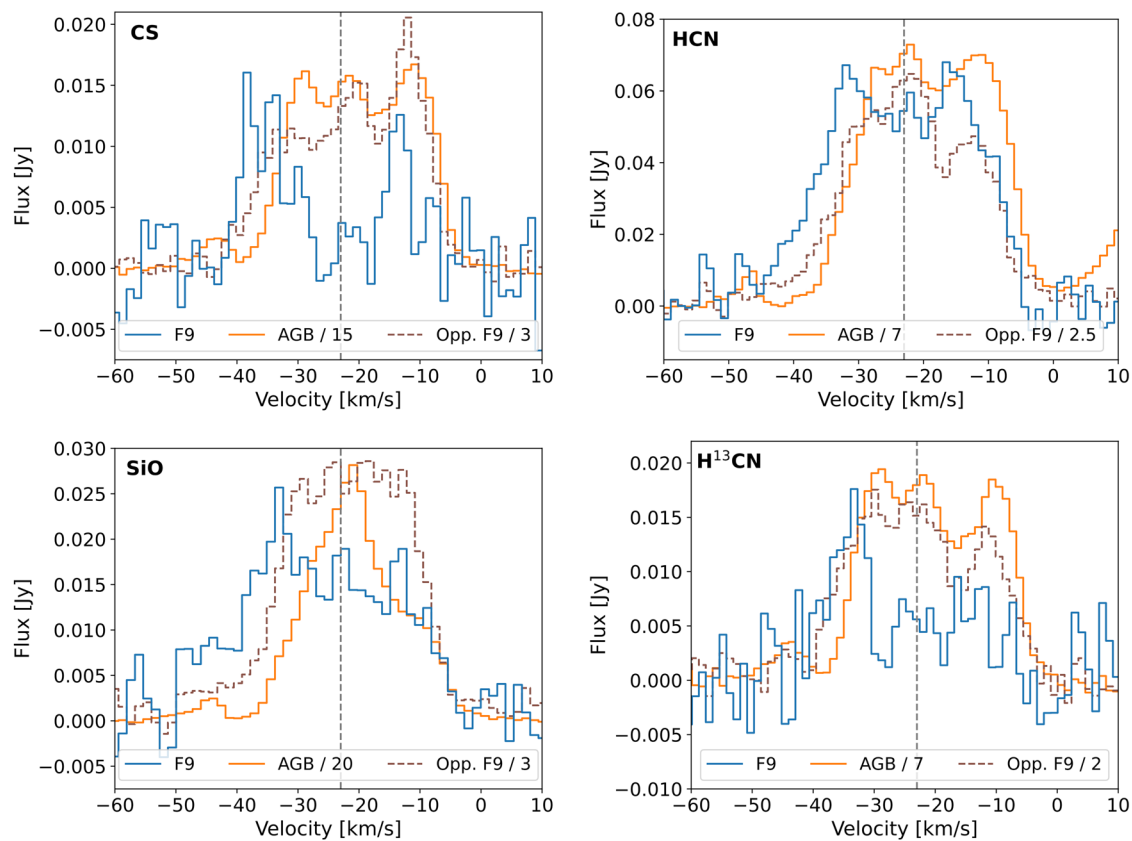
**Extended Data Fig. 3 | Plots of NS towards W Aql.** (a) Zeroth moment map of NS towards W Aql with contours at levels of  $3$  and  $5\sigma$ . North is up and east is to the left. The position of the AGB star is indicated by the red star at  $(0,0)$  and the location of the F9 companion is indicated by the yellow star to the south-west. The white ellipse in the bottom left corner indicates the size of the synthesized beam. (b) Position-velocity diagram of NS taken with the same wide slit as used

for SiN (Fig. 1). The position and LSR velocity of the AGB star is indicated by the red star and the horizontal dotted yellow line indicates the present offset of the F9 star. (c) Spectra of the NS, SiN and SiC lines given in Table 1. All lines were extracted for circular apertures with radii  $0.25''$ , centred on the continuum peak. The flux of the SiC spectrum is multiplied by 5 to allow for a more direct comparison to SiN and NS.



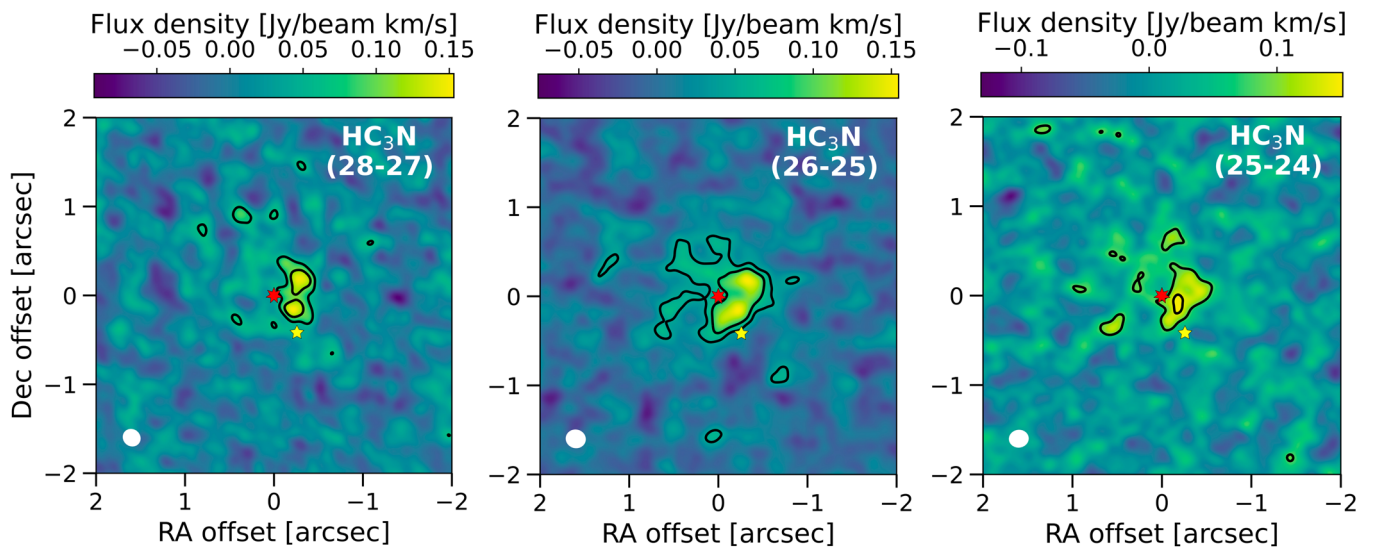
**Extended Data Fig. 4 | Central channels of molecular emission towards W Aql.** A channel of SiS (left) and CS (right) are plotted, showing the asymmetric distribution of these molecules caused by the flux from the F9 star. The positions of the AGB and F9 stars are indicated by the red and yellow stars, respectively. The

channel velocities are given in the top right corners and the beam is shown in the bottom left corner. Contours are plotted for levels of 3, 5, and  $10\sigma$ . North is up and east is left.



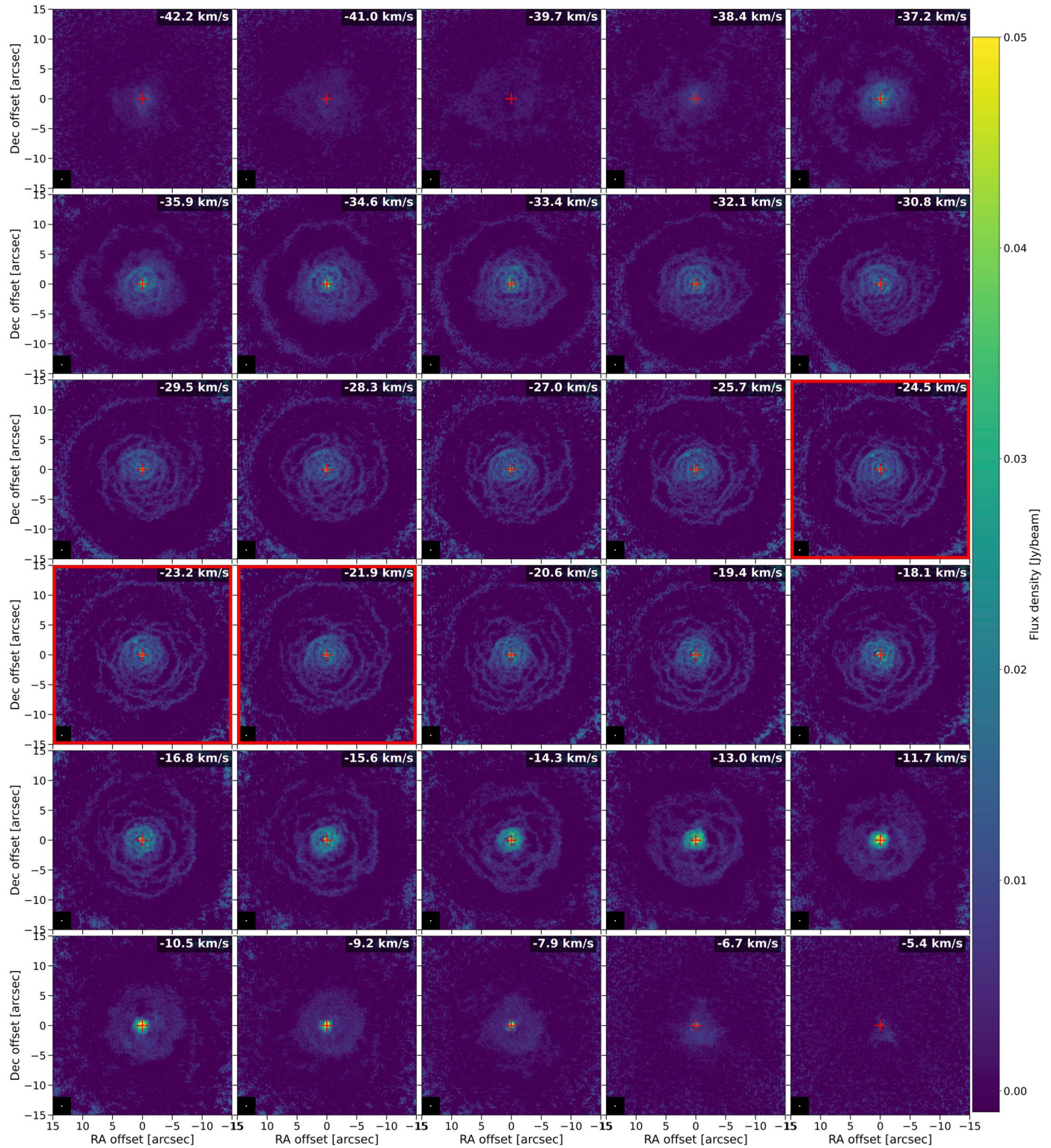
**Extended Data Fig. 5 | A comparison of spectral lines at different locations in the AGB wind.** Plots are shown of CS, HCN, SiO and H<sup>13</sup>CN emission extracted from circular apertures with 100 mas radii centred on the F9 star (blue), on the AGB star (orange) and at the same separation as the F9 star but on the opposite

side of the AGB (Opp. F9, brown, dashed). (See Table 1 for line frequencies.) The AGB and Opp. F9 line profiles are scaled by the factor given in the legend to facilitate comparison with the F9 line profiles. The vertical grey line indicates  $v_{\text{LSR}} = -23 \text{ km s}^{-1}$ .



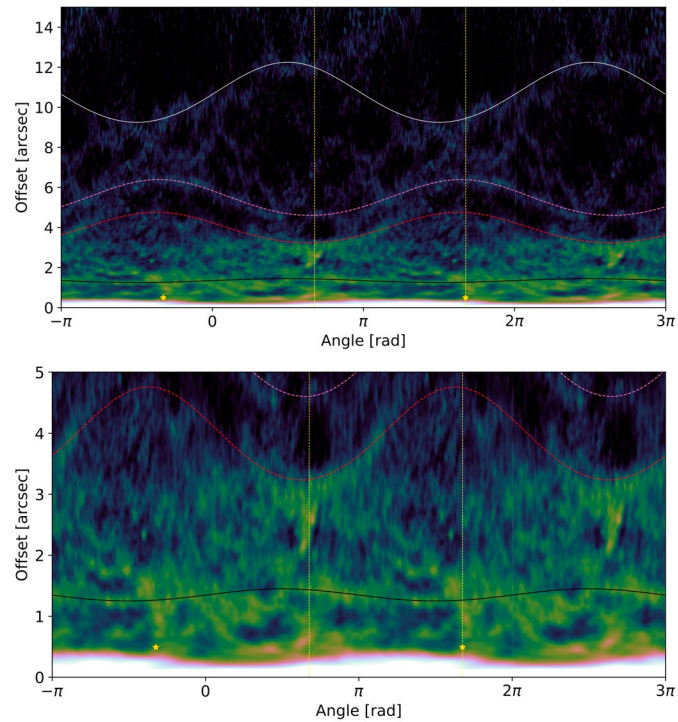
**Extended Data Fig. 6 | Zeroth moment maps of  $\text{HC}_3\text{N}$  towards W Aql.** The transition for each map is given in the top right, with further details given in Table 1. Contours are plotted at levels of  $3$  and  $5\sigma$ . North is up and east is to the left. The position of the AGB star is indicated by the red star at  $(0,0)$ , also corresponding

to the continuum peak, and the location of the F9 companion is indicated by the yellow star to the south-west. The white ellipse in the bottom left corner indicates the size of the synthesized beam.



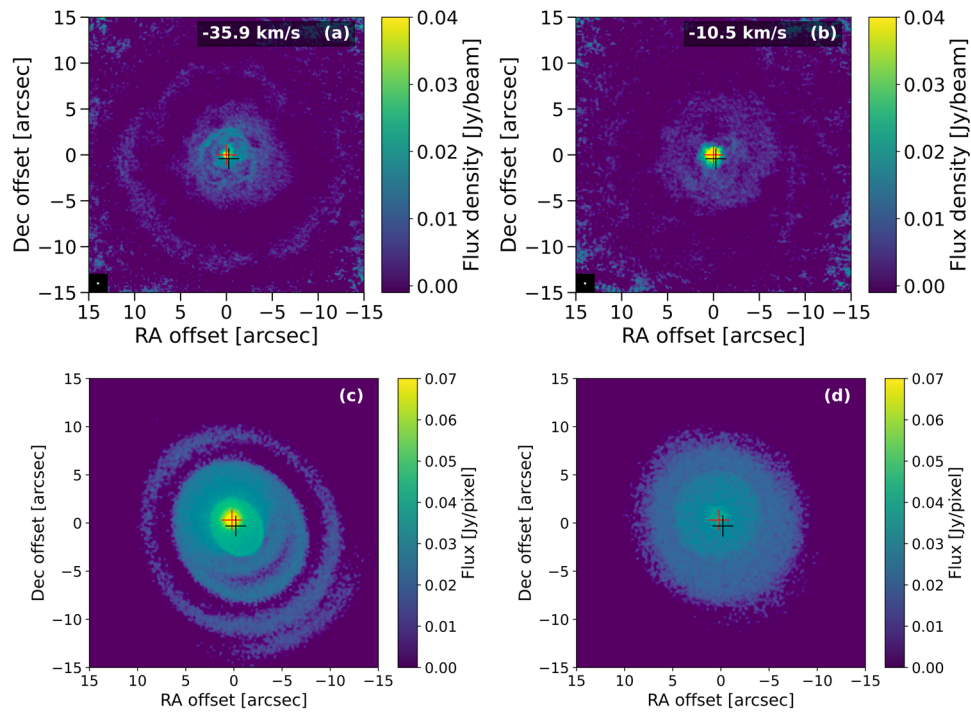
**Extended Data Fig. 7 | CO emission towards W Aql.** Channel maps of CO ( $J=2 \rightarrow 1$ ) are shown towards W Aql, obtained by combining observations from three configurations of ALMA. The AGB star is located at (0,0) and is marked by a red cross. The LSR velocity of each channel is given in the top right hand corner

and the three channels closest to the W Aql  $v_{\text{LSR}} = -23 \text{ km s}^{-1}$  are highlighted with red borders and summed for Fig. 5. The synthetic beam is given by the white ellipse in the bottom left corner of each channel. North is up and east is left.



**Extended Data Fig. 8 | Variations in the radial emission of CO with angle.** The plots show the radial emission distribution against angle for the summed central three channels of CO (Fig. 5) with a full revolution shown in the centre (0 to  $2\pi$ ) and half a revolution is shown on either side ( $-\pi$  to 0 and  $2\pi$  to  $3\pi$ ) to show how the structures extend onwards. The location of the F9 star is indicated by the yellow star and a yellow dotted line which passes through both stars is plotted in

the central winding to guide the eye. The black, red and white curves correspond to the same features highlighted in Fig. 5. The top plot shows the full observed extent of the CO emission (out to  $15''$ ) and the bottom plot focuses on the regions out to  $5''$  from the AGB star. These plots are reproduced without the additional curves in Supplementary Figure 4.



**Extended Data Fig. 9 | Observations and models of blue and red CO emission towards W Aql.** The plots show that blue (a and c) and red (b and d) channels equidistant from the stellar LSR velocity ( $v_{\text{LSR}} = -23 \text{ km s}^{-1}$ ) in velocity space do not exhibit identical CO emission patterns. The ALMA observations (a and b) show an elongated emission region on the blue side (a) and an approximately

round emission region on the red side (b). The same pattern is mimicked in the red (c) and blue (d) channels of the hydrodynamic model processed with MCFOST. The red and black crosses correspond to the locations of the AGB and F9 stars. Note that the modelled and observed positions do not exactly correspond. Details are given in ‘Hydrodynamic simulations’ in the Methods.

## Extended Data Table 1 | Possible orbital solutions for the W Aql system

| $e$  | $r_p$ [cm]           | $r_p$ [au] | $a$ [au] | $T$ [years] | $\Delta t$ [years] | $t_{\text{close}}$ [years] |
|------|----------------------|------------|----------|-------------|--------------------|----------------------------|
| 0.98 | $4.5 \times 10^{13}$ | 3.0        | 150      | 1131        | 157                | 1.9                        |
| 0.97 | $6.5 \times 10^{13}$ | 4.3        | 145      | 1069        | 163                | 3.3                        |
| 0.96 | $8.5 \times 10^{13}$ | 5.7        | 142      | 1038        | 167                | 5.0                        |
| 0.96 | $9.0 \times 10^{13}$ | 6.0        | 150      | 1131        | 165                | 5.4                        |
| 0.95 | $1.1 \times 10^{14}$ | 7.4        | 147      | 1093        | 170                | 7.3                        |
| 0.94 | $1.3 \times 10^{14}$ | 8.7        | 145      | 1069        | 174                | 9.3                        |
| 0.93 | $1.5 \times 10^{14}$ | 10         | 143      | 1051        | 179                | 12                         |
| 0.93 | $1.6 \times 10^{14}$ | 11         | 153      | 1158        | 177                | 13                         |
| 0.92 | $1.7 \times 10^{14}$ | 11         | 142      | 1038        | 183                | 14                         |
| 0.92 | $1.8 \times 10^{14}$ | 12         | 150      | 1131        | 181                | 15                         |
| 0.91 | $1.9 \times 10^{14}$ | 13         | 141      | 1028        | 187                | 16                         |
| 0.91 | $2.0 \times 10^{14}$ | 13         | 149      | 1110        | 186                | 18                         |

Table notes:  $e$  is the eccentricity,  $r_p$  is the periastron,  $a$  is the semimajor axis,  $T$  is the orbital period,  $\Delta t$  is the time since the most recent periastron, and  $t_{\text{close}}$  is the amount of time the two stars spend close together (see 'Orbital solutions' in the Methods).